Mineralium Deposita

# Stable H-C-O isotope and trace element geochemistry of the Cummins Range Carbonatite Complex, Kimberley region, Western Australia: Implications for hydrothermal REE mineralization, carbonatite evolution and mantle source regions

--Manuscript Draft--

| | |
|---|---|
| **Manuscript Number:** | MIDE-D-14-00001R1 |
| **Full Title:** | Stable H-C-O isotope and trace element geochemistry of the Cummins Range Carbonatite Complex, Kimberley region, Western Australia: Implications for hydrothermal REE mineralization, carbonatite evolution and mantle source regions |
| **Article Type:** | Regular Articles |
| **Corresponding Author:** | Peter Downes<br>Western Australian Museum<br>Welshpool DC, Western Australia AUSTRALIA |
| **Corresponding Author Secondary Information:** | |
| **Corresponding Author's Institution:** | Western Australian Museum |
| **Corresponding Author's Secondary Institution:** | |
| **First Author:** | Peter Downes |
| **First Author Secondary Information:** | |
| **Order of Authors:** | Peter Downes |
| | Attila Demény |
| | György Czuppon |
| | A. Lynton Jaques |
| | Michael Verrall |
| | Marcus Sweetapple |
| | David Adams |
| | Neal J McNaughton |
| | Lachland G Gwalani |
| | Brendan J Griffin |
| **Order of Authors Secondary Information:** | |
| **Abstract:** | The Neoproterozoic Cummins Range Carbonatite Complex (CRCC) is situated in the southern Halls Creek Orogen adjacent to the Kimberley Craton in northern Western Australia. The CRCC is a composite, sub-vertical to vertical stock ~2 km across with a rim of phlogopite-diopside clinopyroxenite surrounding a plug of calcite carbonatite and dolomite carbonatite dykes and veins that contain variable proportions of apatite-phlogopite-magnetite ± pyrochlore ± metasomatic Na-Ca amphiboles ± zircon. Early high-Sr calcite carbonatites (4800-6060 ppm Sr; La/YbCN = 31.6-41.5; δ13C = -4.2 to -4.0 ‰) possibly were derived from a carbonated silicate parental magma by fractional crystallization. Associated high-Sr dolomite carbonatites (4090-6310 ppm Sr; La/YbCN = 96.5-352) and a late-stage, narrow, high-REE dolomite carbonatite dyke (La/YbCN = 2756) define a shift in the C-O stable isotope data (δ18O = 7.5 to 12.6 ‰; δ13C = -4.2 to -2.2 ‰) from the primary carbonatite field that may have been produced by Rayleigh fractionation with magma crystallization and cooling, or through crustal contamination via fluid infiltration. Past exploration has focussed primarily on the secondary monazite-(Ce)-rich REE and U mineralization in the oxidised zone overlying the carbonatite. However, high-grade primary hydrothermal REE mineralization also occurs in narrow (<1 m wide) shear-zone hosted lenses of apatite-monazite-(Ce) and foliated monazite-(Ce)-talc rocks (≤~25.8 wt% TREO; La/YbCN = 30085), as well as in high-REE |

| | |
|---|---|
| | dolomite carbonatite dykes (3.43 wt% TREO), where calcite, parisite-(Ce) and synchysite-(Ce) replace monazite-(Ce) after apatite. Primary magmatic carbonatites were widely hydrothermally dolomitized to produce low-Sr dolomite carbonatite (38.5-282 ppm Sr; La/YbCN = 38.4-158.4; δ18O = 20.8 to 21.9 ‰; δ13C = -4.3 to -3.6 ‰) that contains weak REE mineralization in replacement textures, veins and coating vugs. The relatively high δD values (-54 to -34 ‰) of H2O derived from carbonatites from the CRCC indicate that the fluids associated with carbonate formation contained a significant amount of crustal component in accordance with the elevated δ13C values (~ -4 ‰). The high δD and δ13C signature of the carbonatites may have been produced by CO2-H2O metasomatism of the mantle source during Paleoproterozoic subduction beneath the eastern margin of the Kimberley Craton. |
| **Response to Reviewers:** | See the attached file for a detailed response to reviewers comments. |

# Stable H-C-O isotope and trace element geochemistry of the Cummins Range Carbonatite Complex, Kimberley region, Western Australia: Implications for hydrothermal REE mineralization, carbonatite evolution and mantle source regions

Peter J. Downes[1], Attila Demény[2], György Czuppon[2], A. Lynton Jaques[3], Michael Verrall[4], Marcus Sweetapple[4], David Adams[5,6], Neal J. McNaughton[7], Lalchand G. Gwalani[8] and Brendan J. Griffin[5]

[1]Department of Earth and Planetary Sciences, Western Australian Museum, Locked Bag 49, Welshpool DC, Western Australia, Australia. Email peter.downes@museum.wa.gov.au, Ph: +61 8 92123757.

[2]Institute for Geological and Geochemical Research, Hungarian Academy of Sciences, Hungary;

[3]Research School of Earth Sciences, Australian National University, Canberra, A.C.T., Australia;

[4]CSIRO Earth Science and Resource Engineering, Perth, Western Australia, Australia;

[5]Centre for Microscopy, Characterisation and Analysis, University of Western Australia, Australia;

[6]GEMOC, Department of Earth and Planetary Sciences, Macquarie University, NSW, Australia;

[7]John de Laeter Centre for Isotope Research, Curtin University, Western Australia, Australia;

[8]Speewah Research Project C/- King River Copper Limited, B-26/122 Mounts Bay Road, Perth, Western Australia, Australia

## Abstract

The Neoproterozoic Cummins Range Carbonatite Complex (CRCC) is situated in the southern Halls Creek Orogen adjacent to the Kimberley Craton in northern Western Australia. The CRCC is a composite, sub-vertical to vertical stock ~2 km across with a rim of phlogopite-diopside clinopyroxenite surrounding a plug of calcite carbonatite and dolomite carbonatite dykes and veins that contain variable proportions of apatite–phlogopite–magnetite ± pyrochlore ± metasomatic Na-Ca amphiboles ± zircon. Early high-Sr calcite carbonatites (4800–6060 ppm Sr; $La/Yb_{CN}$ = 31.6–41.5; $\delta^{13}C$ = -4.2 to -4.0 ‰) possibly were derived from a carbonated silicate parental magma by fractional crystallization. Associated high-Sr dolomite carbonatites (4090–6310 ppm Sr; $La/Yb_{CN}$ = 96.5–352) and a late-stage, narrow, high-REE dolomite carbonatite dyke ($La/Yb_{CN}$ = 2756) define a shift in the C-O stable isotope data ($\delta^{18}O$ = 7.5 to 12.6 ‰; $\delta^{13}C$ = -4.2 to -2.2 ‰) from the primary carbonatite field that may have been produced by Rayleigh fractionation with magma crystallization and cooling, or through crustal contamination via fluid infiltration. Past exploration has focussed primarily on the secondary monazite-(Ce)-rich REE and U mineralization in the oxidised zone overlying the carbonatite. However, high-

grade primary hydrothermal REE mineralization also occurs in narrow (<1 m wide) shear-zone hosted lenses of apatite-monazite-(Ce) and foliated monazite-(Ce)-talc rocks (≤~25.8 wt% TREO; $La/Yb_{CN}$ = 30085), as well as in high-REE dolomite carbonatite dykes (3.43 wt% TREO), where calcite, parisite-(Ce) and synchysite-(Ce) replace monazite-(Ce) after apatite. Primary magmatic carbonatites were widely hydrothermally dolomitized to produce low-Sr dolomite carbonatite (38.5–282 ppm Sr; $La/Yb_{CN}$ = 38.4–158.4; $\delta^{18}O$ = 20.8 to 21.9 ‰; $\delta^{13}C$ = -4.3 to -3.6 ‰) that contains weak REE mineralization in replacement textures, veins and coating vugs. The relatively high δD values (–54 to –34 ‰) of $H_2O$ derived from carbonatites from the CRCC indicate that the fluids associated with carbonate formation contained a significant amount of crustal component in accordance with the elevated $\delta^{13}C$ values (~ -4 ‰). The high δD and $\delta^{13}C$ signature of the carbonatites may have been produced by $CO_2$-$H_2O$ metasomatism of the mantle source during Paleoproterozoic subduction beneath the eastern margin of the Kimberley Craton.

**Keywords**

Carbonatite, REE mineralization, H-C-O stable isotopes, phoscorite, clinopyroxenite, monazite-(Ce), Kimberley

# Introduction

The Neoproterozoic Cummins Range Carbonatite Complex (CRCC) is situated at the southern apex of the Halls Creek Orogen, close to its junction with the King Leopold Orogen, adjacent to the Kimberley Craton in northern Western Australia (lat. 19º27'S, long. 127º10'E; Fig. 1). The CRCC is defined by a major magnetic anomaly and comprises a composite, sub-vertical to vertical zoned stock in which a phlogopite-diopside clinopyroxenite was intruded by calcite carbonatite and dolomite carbonatite dykes and veins that contain variable proportions of apatite–phlogopite–magnetite ± pyrochlore ± metasomatic Na-Ca amphiboles ± zircon (Fig. 2).

Past company exploration has focussed on the oxidised zone above the carbonatite which contains a REE ore body with an inferred resource of 4.90 Mt at 1.74% TREO, 11.2% $P_2O_5$ and 145 ppm $U_3O_8$ (Kimberley Rare Earths 2012). This monazite-(Ce)-apatite-rich secondary ore largely formed through the mechanical concentration of primary magmatic–hydrothermal REE mineralization within the carbonatite during weathering and deflation. The ore body is the third largest REE resource in Western Australia behind the Mt Weld deposit and the Hastings-Brockman trachytic tuff (Geological Survey of Western Australia 2011).

In this paper we employ H-C-O stable isotope and whole-rock geochemistry to define the evolution of various phases of the Cummins Range carbonatite and associated hydrothermal–metasomatic processes involved in REE mineralization. H-C-O isotope data also provides information on the development of the mantle source regions for the CRCC where previous work has indicated the influence of subduction-related processes and the existence of a Neoarchean depleted lithospheric mantle root beneath the Halls Creek Orogen (Jaques et al. 1989a; Luguet et al. 2009; Honda et al. 2012).

## Geological setting

The Paleoproterozoic Halls Creek Orogen is comprised of a NNE-trending band of deformed and metamorphosed sedimentary, volcanic and intrusive rocks that represents a suture zone between the Kimberley Craton and the remainder of the North Australian Craton to the east (Fig. 1). Amalgamation following plate collision had occurred by ~1820 Ma (Myers et al. 1996; Tyler et al. 1999; 2012; Griffin et al. 2000; Cawood and Korsch 2008; Richards 2013). The Argyle lamproite, associated lamproite dykes and the Bow Hill ultramafic lamprophyre dykes were emplaced along a terrane boundary within the Halls Creek Orogen during the Proterozoic (Fig. 1; Jaques et al. 1986; Jaques and Milligan 2004). Similarly, a deep crustal structure within the King Leopold Orogen probably provided a route for lamproite magmas to reach the surface during the Miocene (~17–22 Ma) volcanism in the West Kimberley (Ellendale; Fig. 1; Jaques and Milligan 2004). The Cummins Range Carbonatite Complex has been interpreted by a number of workers to be emplaced in the proximity of the Halls Creek Fault (Fig. 1; e.g. Sanders 1999). Country rocks, including granite gneiss and chlorite schist, are interpreted to be part of the Eastern zone of the Paleoproterozoic Lamboo Complex within the Halls Creek Orogen (Fig. 2; Andrew 1990; cf. Hassan 2000). The contacts of the CRCC are largely inferred from magnetic data and no structural disruption or contact metamorphism was found on the margins of the carbonatite complex. Neoproterozoic ages of ~854–1012 Ma (currently under review) are indicated for the CRCC by dating using various methods (Pidgeon et al. 1986; Sun et al. 1986).

## Outline of Geology

Previous detailed accounts of the geology and mineralogy of the intrusive complex may be found in Richards (1983, 1985) and Andrew (1990). The CRCC has little surface expression, with the area largely being concealed by an aeolian sand sheet of varying thickness, typical of the Great Sandy Desert. Exposure is limited to patchy outcrop of low mounds of jasperoidal matrix-supported ironstone breccia, interpreted to be a residual solution collapse breccia of karst origin (Fig. 2; Richards 1983). Other regolith units noted within, or beneath sand cover, are ferruginous laterite, silcrete and calcrete. Resistate minerals, including REE-bearing monazite-(Ce), apatite, zircon and pyrochlore are considered to have been enriched by up to 10 times their original concentration in the oxidised zone (Andrew 1990), but the nature of this enrichment is not well defined.

Drilling and aeromagnetic and more detailed ground magnetic surveys have shown that the CRCC is a composite, sub-vertical to vertical stock some 1.8 x 1.6 km in maximum dimensions with three broadly concentric zones (Fig. 2). A central intrusive zone or plug of calcite carbonatite and dolomite carbonatite dykes is surrounded by variably carbonated and metasomatically altered phlogopite clinopyroxenite. Adjacent to the central carbonatite intrusive zone the clinopyroxenite was intruded by numerous steeply-dipping carbonatite dykes up to ~60m thick and metasomatism of the clinopyroxenite by the carbonatite is most intense in this zone, where there is a high density of carbonate veins/microveins and invasion of the clinopyroxenite by carbonatite (Andrew 1990). The outer envelope

comprises less altered clinopyroxenite with a mineral assemblage that includes phlogopite, diopside, apatite, magnetite, calcite and ilmenite, and lesser amounts of metasomatic Na-Ca amphiboles and accessory zirconolite (Table 1; Fig. 2). Sulfide ± oxide assemblages composed of pyrrhotite, pyrite, chalcopyrite, ± sphalerite ± galena ± magnetite are common to both the clinopyroxenite and various phases of the carbonatite, where they may form sulfide-rich bands and lenses. Within the carbonatite, vugs up to several centimetres wide commonly contain hydrothermal pyrite, marcasite and chalcopyrite (Table 1). Sulfides exhibit textures that suggest that they have formed through the replacement of carbonates (calcite and dolomite), diopside (or actinolite), to a lesser extent apatite, and rarely monazite-(Ce).

The carbonatite and clinopyroxenite are cut by vertical–sub vertical shear zones, trending ~315–330˚, that include weakly to strongly foliated dolomite carbonatite, zones of phlogopitite, and zones of high-REE apatite-monazite-(Ce) rock (Fig. 3). Some shear zones have been localised along contacts between the clinopyroxenite and carbonatite and this deformation may have played a major role in producing foliated phlogopitite along the margins of some clinopyroxenite bodies. This apparent K-metasomatism does not appear to have been entirely related to contact metasomatism with the intrusion of carbonatite into clinopyroxenite, because zones of phlogopitite are asymmetric in distribution. At some boundaries of the clinopyroxenite there are quite thick zones of phlogopitite (≤~10 m), but at others minimal phlogopitite is developed (cm-scale). This suggests a correlation with zones of shearing. The shear zone trend of ~315–330˚ may also be reflected in the approximate orientation of the outcrop of iron oxide collapse breccias (Fig. 2) and the orientation of the REE orebody within the oxidised zone (see Appendix 1).

## Analytical methods

Scanning electron microscopy and electron microprobe microanalysis

Mineral identifications were assisted by detailed back-scattered electron (BSE) imaging and energy-dispersive X-ray spectrometry (EDS) using a Philips XL-40 scanning-electron microscope (SEM) at CSIRO Earth Science and Resource Engineering, Perth.

The composition of apatite was determine at the Centre for Microscopy, Characterisation and Analysis at the University of Western Australia using a field emission gun JEOL JXA-8530F Hyperprobe with five wavelength-dispersive spectrometers operating at 20 keV, 50 nA, and a 10 μm diameter beam to minimise fluorine diffusion. All analyses were performed using the Probe for EMPA software by Probe Software, Inc. F and Ca were analysed first using a Time Dependent Intensity (TDI) correction to account for any anisotropic elemental diffusion during analysis. REEs were standardised using the Smithsonian Institution single element orthophosphate standards. Ca and F were standardised on Durango apatite; Cl was standardised on a Brazilian sodalite. Natural orthoclase was used as the standard for Si and K, and San Carlos olivine was used for Fe calibration. Sr was calibrated on synthetic celestine and synthetic barite was used for S. Standards used for U, Th, and Pb were U metal, $ThO_2$, and crocoite respectively. All REEs, Th, and U were counted for 100 seconds on peak and major elements were counted for 10 – 40 seconds on peak. All elemental peak overlaps were accounted for and eliminated using software peak overlap correction routines. Errors on all elements are $\leq 10\%$.

178

179 Whole-rock geochemistry

180

181 Abundances of major and trace elements were determined at Geoscience Australia,
182 Canberra by XRF and ICP-MS for selected samples. Major and minor elements (Si, Ti, Al,
183 Fe, Mn, Mg, Ca, Na, K, P and S) were determined by wavelength-dispersive (Bruker
184 S8Tiger) XRF on fused disks using methods similar to those of Norrish and Hutton
185 (1969). Precision for these elements is better than ±1% of the reported values. As, Ba, Cr,
186 Cu, Ni, Sc, V, Zn, Zr, F and Cl were determined by XRF on pressed pellets using methods
187 similar to those described by Norrish and Chappell (1977). Loss on Ignition (LOI) was by
188 gravimetry after combustion at 1100$^{o}$C. FeO abundances were determined by digestion and
189 electrochemical titration using a modified methodology based on Shapiro and Brannock
190 (1962), and $Fe_2O_3$ values were calculated as the difference between total Fe, determined by
191 XRF, and FeO. Selected trace elements (Cs, Ga, Nb, Pb, Rb, Sb, Sn, Sr, Ta, Th, U, Y) and
192 the Rare Earth elements were analysed by ICP-MS (Agilent 7500 with reaction cell) using
193 methods similar to those of Eggins et al. (1997), but on solutions obtained by dissolution of
194 fused glass disks (Pyke 2000). Precisions are ±5% and ±10% at low levels (<20 ppm).
195 Agreement between XRF and ICP-MS are typically within 10%. Because of problems in
196 retaining the sample in solution, the REE and F-rich fused XRF disc of sample CDD1-36
197 (and CDD1-34 for comparison) was also analysed by laser ablation ICP-MS at the
198 Research School of Earth Sciences, ANU, for REEs and other trace elements using an
199 Agilent Technologies 7700 ICP-MS coupled to an ANU HelEX laser-ablation system with
200 a 193 nm wavelength EXCIMER laser (110 (ArF) COMPex, Lambda Physik) following the

method of Jenner and O'Neill (2012). Data acquisition involved a 20 second background measurement followed by 45 seconds of ablation, employing an 81 micron diameter laser spot, 5 Hz repetition rate and 50-55 mJ fluence. Samples were analysed by bracketing every 5 unknowns with analyses of NIST610 and BCR2G reference glasses. Data were processed using the Iolite software package (Paton et al. 2011). Agreement of the LA-ICP-MS and solution ICP-MS methods for sample CDD1-34, and with recommended/preferred values for standards BCR-2G and SY-3 was within 10% for most elements at the ppm level and higher. LA-ICP-MS data for the REEs, Zr, Hf, Ta, Th and U in sample CDD1-36, and Tm, Hf and Ta in sample CDD1-34, are therefore reported here.

Abundances of trace elements for 9 rock samples were determined at TSW Analytical, Perth (analyst Sven Fjastad) using a combination of ICP-MS (Agilent 7700) and ICP-AES (Thermo Scientific iCAP) analysis. Solutions for analysis were prepared by two methods: (a) The pulverised sample (0.3 g) was fused with lithium tetraborate (35.3%)/lithium metaborate (64.7%) flux (0.8 g) at 1050˚C for 15 minutes, then the fused material was dissolved in a citric acid solution (50 mL, 10% m/v); and (b) The pulverised sample (0.25 g) was digested in a mixture of nitric, perchloric and hydrofluoric acids. The digestate was taken to incipient dryness and the residue dissolved in a mixture of nitric and hydrochloric acid then diluted with ultra-pure water to produce a final acid strength of ~5% v/v. The resultant solutions were then diluted appropriately for ICP-AES and ICP-MS analysis.

The elements reported for these samples have been compiled from, and confirmed by, using both the ICP-AES and ICP-MS results from the above sample preparation techniques. The detection limits vary from element to element in the various solution matrices and instrumental technique used, however as a generalisation elements reported from the ICP-

AES assay have limits of detection (2σ) of approximately 10 ppm in the pulverised sample and elements reported from the ICP-MS assay have limits of detection (2σ) of approximately 0.1 ppm in the pulverised sample.

Stable Isotopes

For carbonate samples from the CRCC the stable carbon and oxygen isotope compositions were determined by applying the carbonate-orthophosphoric acid reaction at 72ºC (Spötl and Wennemann 2003) and using an automated GASBENCH II sample preparation device attached to a Thermo Finnigan Delta Plus XP mass spectrometer at the Institute for Geological and Geochemical Research, Budapest, Hungary.

Hydrogen isotope compositions of fluid inclusion-hosted $H_2O$ and $H_2O$-contents in ten carbonate samples were determined by vacuum-crushing followed by $H_2O$ purification by vacuum distillation, reaction with Zn at 480ºC to produce $H_2$ gas and mass spectrometric analyses of D/H ratios (see Demény 1995, Demény and Siklósy 2008, Czuppon et al. 2014) using a Finnigan MAT delta S mass spectrometer at the Institute for Geological and Geochemical Research.

The isotope compositions are given as δD, $\delta^{13}C$ and $\delta^{18}O$ in parts per thousands (‰) relative to V-PDB ($\delta^{13}C$) and V-SMOW (δD and $\delta^{18}O$), according to the equation: $\delta = (R_{sample}/R_{standard}-1) \times 1000$, where R is the D/H, $^{13}C/^{12}C$ or $^{18}O/^{16}O$ ratio in the sample or in the international standard. The measurement precision is better than 0.15‰ for C and O isotope data based on replicate measurements of international standards (NBS-19; NBS-

18) and in–house reference materials. Reproducibilities of H isotope analyses were about 3‰ for δD values based on duplicate analyses.

Two samples of the high-REE apatite-monazite-(Ce) rock (CDD1-31, CDD1-37A) were examined and found not to contain fluid inclusions.

## Petrography

Fresh rocks within the Cummins Range complex were encountered in two deep inclined diamond drill holes, CDD1 and CDD2, each ~402 m long (Figs 2, 3; Appendix 1). The petrographic descriptions presented here are based mostly on samples from these drill holes. Most exploration drilling has concentrated on defining the shallow REE resource within the oxidised zone. Two of the samples analysed for C-O isotopes came from shallow RC drill holes (NRC035 92–93 m, NRC058 97–98 m). We describe the various carbonatites and the high-REE apatite-monazite-(Ce) rock in detail here, but the associated clinopyroxenite will be described elsewhere (Table 1).

We use the term ‘phoscorite’ to describe apatite-amphibole-rich rocks that also contain varying proportions of phlogopite, magnetite, dolomite, ± calcite ± ilmenite (Table 1). No olivine-bearing rocks have been found in the CRCC. The definition of ‘phoscorite’ or ‘phoscorite-series’ rocks is complex, and this is discussed in detail by Krasnova et al. (2004).

## Carbonatites

Multiple phases of calcite carbonatite and dolomite carbonatite dykes intruded the clinopyroxenite phase of the CRCC producing a central carbonatite plug (Fig. 2). The carbonatites contain variable proportions of apatite ± phlogopite ± magnetite ± amphibole, and with increasing content of these minerals range towards silicocarbonatites or phoscorite-series rocks (Table 1; Fig. 4). Blue-green, Na-Ca amphiboles (predominantly richterite) are a metasomatic phase (≤~5 vol.%) that overprint the magmatic carbonatite rock fabric, including replacement of phlogopite and apatite (Fig. 4b, c). Contact relationships between carbonatites and associated phoscorite-series rocks commonly are gradational. Fresh diopside has not been observed in the carbonatites at Cummins Range, however diopside may have been a primary magmatic phase that has been replaced by richterite in associated apatite-amphibole-rich phoscorite.

The carbonatites vary from fine to coarse-grained, and from massive to foliated. The foliated textures indicate ductile deformation of the carbonatite during tectonism (Fig. 4d). Generally, the carbonatites are either calcite or dolomite dominant, where the carbonates comprise up to ~95 vol.% of the rock. Recrystallization and hydrothermal alteration of the carbonatites has produced massive, turbid, microporous dolomite or calcite in some zones. In the carbonatites, apatite occurs as individual equant to elongate crystals (≤1.5 cm long) or as radiating to divergent clusters of elongate crystals (≤4 cm across) generally situated at calcite or dolomite grain boundaries, or in lenses of polygonal crystal cumulate (Fig. 4c). Pyrochlore and zircon are characteristic minor accessory minerals. Pyrochlore (generally <1 vol.%) occurs as equant, euhedral to anhedral, dark brown to golden brown crystals

≤10mm wide. It is commonly overgrown by thin rims of pyrite, and very rarely is replaced by ferrocolumbite. Zircon exhibits a diverse range of textures including subhedral megacrysts to ~1.5cm wide with typical igneous growth zonation (Fig. 4a; occurring in CDD1 323–331 m), anhedral, metamict composite porphyroblasts intergrown with dolomite in strongly foliated carbonatite (≤3 mm wide; Fig. 4d), and turbid brown anhedral–subhedral crystals intergrown with amphibole-ilmenite-apatite-dolomite (≤5 mm wide). Textural relationships indicate that the zircon is variably igneous to hydrothermal or metasomatic in origin. The zircons have a very low U content (≤138 ppm; unpubl. data NJ McNaughton) consistent with their carbonatite origin (cf. Belousova et al. 2002).

Carbonatites within the CRCC commonly contain trace–minor hydrothermal REE-mineralization (generally <1 vol.%) in the form of disseminated grains of monazite-(Ce), parisite-(Ce) and synchysite-(Ce) in calcite and dolomite; monazite-(Ce) rimming and replacing magmatic apatite; parisite-(Ce) and synchysite-(Ce) in replacement textures, veins and lining cavities in carbonatite; as well as minor nioboaeschynite-(Ce), chevkinite-(Ce), fergusonite and Ca-REE-Ba-Sr carbonates (possibly burbankite or carbocernaite; Fig. 5).

*High-Sr calcite carbonatite*

Calcite carbonatites may have a fine-grained, equigranular to inequigranular polygonal mosaic texture (with straight to slightly curved grain boundaries; crystals ≤1 mm wide), but vary to inequigranular textures where carbonate crystals (≤5 mm long) have irregular to

312 serrated boundaries. White–light grey, massive carbonatite may be intruded (and/or
313 replaced?) by dykes or irregular bodies of light pink calcite carbonatite that occurs only in
314 the drill hole CDD1 (Fig. 4a). This calcite carbonatite may contain minor subhedral to
315 anhedral, phenocrysts and crystal clusters of white dolomite (≤~5 mm long; <15 vol.%) in a
316 calcite groundmass (Fig. 4a). High-Sr calcite carbonatite near the bottom of drill hole
317 CDD2 preserves calcite-dolomite exsolution textures. Small blebs and rods of dolomite
318 (≤~20 μm long) have exsolved from high-Mg calcite.

319

320 *High-Sr dolomite carbonatite*

321

322 White, massive, weakly–moderately fractured dolomite carbonatite is present in both drill
323 holes (e.g. CDD1 150.45–152.26 m; CDD2 ~110–115 m). Generally, it has indistinct
324 contacts with surrounding calcite carbonatite, but is intruded by pink high-Sr calcite
325 carbonatite. The texture varies from zones of inequigranular, variably clear to turbid
326 dolomite, with crystals up to ~2 mm wide having straight to curved or rounded boundaries,
327 grading into a more coarse-grained turbid dolomite with elongated–anhedral crystals
328 ≤~1.25 cm long. This dolomite carbonatite contains rare parisite-(Ce), synchysite-(Ce) and
329 monazite-(Ce) (<1 vol.%). Minor patches and crystals of calcite exhibit microporosity and
330 contain inclusions of strontianite and Ca-REE-Ba-Sr minerals (possibly burbankite or
331 carbocernaite; ≤30 μm long).

332

*High-REE dolomite carbonatite dykes*

Late-stage, thin, grey dolomite carbonatite dykes intrude calcite and calcite-dolomite carbonatite over two intervals within the drill hole CDD2. These dykes contain relatively high-grade REE mineralization (e.g. CDD2 396.9–397.64 m – 3.43 wt% TREO) and their texture and mineralogy are as follows:

1) The grey, medium-grained dolomite carbonatite dyke intruding calcite-dolomite carbonatite over the interval CDD2 225.03–225.23 m, contains turbid dolomite and parisite-(Ce) (~15–20 vol.%; elongate crystals ≤3 mm) with minor aeschynite-(Ce) (crystals ≤~0.8 mm long), monazite-(Ce) and pyrite (Fig. 5a, b). Crystals of parisite-(Ce) are partially resorbed or altered and fractured, with dissolution along cleavage planes. Pyrite (crystals ≤~0.6 mm long) commonly occurs along fractures and cleavage planes in crystals of parisite-(Ce).

2) Dolomite carbonatite dykes intrude calcite carbonatite over the interval CDD2 396.9–397.18 m, 397.35–397.64 m. The REE mineralization in these dykes comprises fine-grained monazite-(Ce), parisite-(Ce) and synchysite-(Ce) in irregularly-shaped patches of pink calcite up to 2 cm long (Fig. 5c, d). Crystals of apatite may be partially to completely replaced by this calcite-REE-rich association (Fig. 5d). These calcite-monazite-(Ce) patches are not restricted to these dykes and occur in less abundance in surrounding calcite carbonatite. The sequence of replacement was apatite replaced by monazite-(Ce) that was later replaced by pink calcite and associated parisite-(Ce) and synchysite-(Ce). Monazite-(Ce) is also rarely replaced by pyrrhotite and magnetite in

this carbonatite. The dolomite carbonatite contains patches and crystals of microporous calcite with microinclusions (<2 μm wide) of strontianite ± Ca-REE-Ba-Sr carbonates (possibly burbankite or carbocernaite).

*Low-Sr dolomite carbonatite*

The low-Sr dolomite carbonatites are white–grey, massive and dominantly composed of turbid recrystallised, microporous dolomite (≤2 cm long crystals; anhedral with irregular boundaries). Boundaries with the surrounding calcite carbonatite commonly are gradational. Some zones within the carbonatite dykes have a vuggy texture and are weakly mineralised (e.g. 110.5–136.4 m, 303–322.2 m in CDD1; 328.3–396 m in CDD2; Fig. 5e). Vugs (≤~5 cm wide), typically containing ≤1 vol.% REE-bearing minerals, are lined by euhedral coarse dolomite crystals associated with crystals of pyrite–marcasite, quartz, monazite-(Ce), encrustations of very fine-grained platy crystals and crystal groups of the REE-fluorocarbonates parisite-(Ce) and synchysite-(Ce) (+ rare fine acicular groups of a Nb-Ti mineral, probably nioboaeschynite-(Ce)) ± Mg-silicates (talc; Fig. 5f).

High-REE apatite-monazite-(Ce) rock

Within the drill hole CDD1, the interval 261.85–275.2 m is composed of weakly–strongly foliated rocks including carbonatite and apatite-monazite-(Ce)-amphibole-talc-rich rocks.

Some strongly foliated zones contain ~5–10 vol.% fine–medium grained disseminated zircon (the zircon has yellow SW fluorescence; ~269–269.15 m, 272.5–273 m). This shear zone was intruded by white, massive–fractured dolomite carbonatite dykes and veins, and over the interval 269.2–271.1 m light grey, fine-grained high REE apatite-monazite-(Ce) rocks (containing ≤~25.8 wt% TREO) occur adjacent to these dolomite carbonatite dykes (≤0.142 wt% TREO; Fig. 6). From historical exploration geochemistry, the interval 269–271m is particularly high grade, with 8.29 wt% from 269–270m, and 5.14 wt% TREO from 270–271 m (Fig. 3). The apatite-monazite-(Ce) rocks comprise complex intergrowths of apatite and monazite-(Ce) (that varies from thin, elongated crystals to granular in habit) that are overprinted by veins of talc-amphibole-pyrrhotite-dolomite (Fig. 7). Monazite-(Ce) may also occur in a talc–amphibole matrix. The thin, elongated crystals of monazite-(Ce) intergrown with apatite are up to ~0.8 mm long, and the apatite in this association is polycrystalline (variation in extinction angle), turbid and partially altered. In one sample (CDD1-33), this apatite-monazite-(Ce) zone has a sharp contact with an adjacent apatite-rich vein containing patchy to concentrically-zoned, elongated, crystals of apatite (≤3 mm long) aligned approximately perpendicular to the vein margins (Fig. 6).

Zones of foliated apatite-talc-monazite-(Ce)-amphibole rock are banded on a cm-scale (e.g. CDD1 265–266 m 3.3 wt% TREO). These include weakly foliated, monazite-(Ce)-talc-rich bands that contain ~40–50 vol.% anhedral–subhedral monazite-(Ce) crystals (≤~1.3 mm long, commonly fractured) in a talc-amphibole-pyrrhotite matrix (Fig. 7b, d). The monazite-(Ce)-talc bands are enclosed by moderately foliated bands of apatite-amphibole-monazite-(Ce)-talc in which the fabric is defined by crystals of green-blue amphibole (richterite, ≤~1.2 mm long) intergrown with fine-grained talc and irregular

lenses and grains of pyrrhotite (≤~1.3 mm long). The amphiboles enclose lenses of recrystallised and altered apatite to ~2 mm long, and trains of equant/granular crystals of monazite-(Ce) (≤~0.7 mm long, ≤~5 vol.%). Banding also includes more massive zones of altered and recrystallised apatite that are crosscut by lenses of amphibole (~15 vol.%, ≤~4 mm long) and ragged grains and lenses of pyrrhotite ± rare chalcopyrite (≤~0.7 mm long).

## Geochemistry

Apatite chemistry

Electron microprobe data acquired from two samples of the high-REE apatite-monazite-(Ce) rock (CDD1-29, CDD1-33) and 3 samples of carbonatite are presented in Table 2 and Fig. 8. The high-REE apatite-monazite-(Ce) rock contains areas with zoned apatite crystals (~5 vol.%). Crystal cores, to ~600 µm long, occur in areas of massive uniform apatite in a talc-rich matrix. Apatite cores are REE-rich ($Y_2O_3$ 0.22–0.43 wt%; TREO 4.07–10.1 wt%; SrO 1.22–2.81 wt%) and apatite rims or surrounding apatite in the matrix are Sr-rich (SrO 1.78–11.39 wt%) and poor in REEs (TREO ≤2.92 wt%; $Y_2O_3$ ≤0.12 wt%). Notably, some of these apatite cores exhibit positive Eu anomalies (Eu/Eu*~2.4–8.8; Fig. 8b). Apatite in the carbonatites has distinctive Sr and REE contents, with generally <2 wt% SrO and ≤2.42 wt% TREO. Apatite analyses from the high-REE apatite-monazite-(Ce) rock may have low

419 analytical totals which could be due to the effects of hydrothermal alteration or the presence
420 of $CO_3^{2-}$ that has not been determined (Table 2; cf. DeToledo et al. 2004).

421

422 Whole-rock geochemistry

423

424 Whole-rock geochemical data for the CRCC is presented in Tables 3 and 4, and Figs 3 and
425 9 (see also Appendix 1). The high-Sr calcite carbonatite contains from 4800–6060 ppm Sr,
426 from 1.41–3.2 wt% MgO, from 0.18–0.30 wt% MnO, and from 0.42–1.80 wt% $P_2O_5$. The
427 calcite carbonatites are weakly mineralised, containing 0.138–0.163 wt% TREO ($La/Yb_{CN}$
428 = 31.6–41.5; $La/Nd_{CN}$ = 1.72–2.23). The pink calcite carbonatite (CDD1-24) has relatively
429 higher Zr and Hf content than other calcite carbonatite samples (Fig. 9b).

430 The high-Sr dolomite carbonatite contains relatively high MnO from 0.683–1.12 wt%,
431 and MgO from 16.1–19 wt% (CDD1-34 contains 12.7 wt% MgO but this sample has a high
432 iron content due to sulfides). Sr content ranges from 4090–6310 ppm, and $P_2O_5$ from 0.1–
433 0.92 wt%. The TREO content is the lowest of all carbonatites in the complex, ranging from
434 0.071–0.145 wt%, but it exhibits high LREE/HREE ratios ($La/Yb_{CN}$ = 96.5–352; $La/Nd_{CN}$
435 = 2–3.14). In contrast, the low-Sr dolomite carbonatite (Sr = 38.5–282 ppm) contains lower
436 amounts of Fe and Mn, but higher TREO (MnO = 0.26–0.34 wt%; $P_2O_5$ = 0.035–0.9 wt%;
437 TREO = 0.124–0.358 wt%). The low-Sr dolomite carbonatite has variable REE content,
438 with $La/Yb_{CN}$ = 38.4–158.4 and $La/Nd_{CN}$ = 1.98–2.73.

439 The high-REE dolomite carbonatite (2) dyke (CDD2-25A) contains 3.43 wt% TREO.
440 It has relatively high $P_2O_5$ (7.28 wt%) due to its apatite content and very high LREE

441 enrichment ($La/Yb_{CN}$ = 2756; $La/Nd_{CN}$ = 5.8). Unfortunately, insufficient sample was
442 available from the high-REE dolomite carbonatite (1) dyke to undertake whole-rock
443 geochemistry. The high-REE apatite-monazite-(Ce) rock (CDD1-36) is rich in Ca, Sr, and
444 P and is extremely enriched in REEs with ~25.8 wt% TREO, has a high $La/Nd_{CN}$ ratio
445 (~5.4), an extremely high $La/Yb_{CN}$ ratio (30085), and a high abundance of Y (126 ppm).
446 Notably, its chondrite-normalised REE pattern is discordant to the quasi-parallel patterns of
447 the carbonatites sampled (Fig. 9a).

448 Geochemically the primary carbonatites are high in Sr, and relatively low in Ba (≤509
449 ppm) and all carbonatites are low in HFSE (e.g. Zr ≤279 ppm, Nb ≤254 ppm, Hf ≤3.81
450 ppm, Ta ≤7.39 ppm). The Th/U, Nb/Ta and Zr/Hf ratios of the carbonatite samples are
451 quite variable (Table 3) and probably are controlled by zircon and pyrochlore content (Fig.
452 9). In four carbonatite samples Hf content is below detection limits and two carbonatites
453 have anomalously low Zr/Hf ratios with Hf content <0.15 ppm (Table 4). The remaining
454 carbonatite samples have Zr/Hf ratios in the range 25.9–73.2 (average ~43.8), which is
455 similar to the range for the Kovdor and Turiy Mys carbonatites from the Kola Alkaline
456 Province, Russia (36–72; Ivanikov et al. 1998; Verhulst et al. 2000) and exceeds the
457 primitive mantle value (~37). The Zr/Hf ratio of the apatite-amphibole phoscorite (52.5) is
458 similar to the worldwide average of phoscorites and silicocarbonatites (57;
459 Chakhmouradian 2006). The average Zr/Nb ratio of the carbonatites is the same as the
460 worldwide carbonatite average (0.8; Chakhmouradian 2006), and much lower than the
461 Zr/Nb ratio of the phoscorite (~6.39).

462 Y/Ho ratios are close to the primitive mantle value (~27) for the majority of carbonatite
463 samples (21.5–27.1), but the high-Sr calcite carbonatite (CDD2-21A) has Y/Ho = 15.1 and

464 the high-REE dolomite carbonatite dyke (2; CDD2-25A) has a low value of 2.14 and a
465 negative Eu anomaly (Eu/Eu* = 0.62). The high-REE apatite-monazite-(Ce) rock (CCD1-
466 36) also has a relatively low Y/Ho ratio of 17.9.

467 Ga/Ge ratios in a large group of calcite and dolomite carbonatites (n = 6) are on
468 average 5.34 (Table 4), which is slightly above the ratio for the primitive mantle ~3.67.
469 Higher Ga/Ge ratios occur in samples with Al-bearing minerals, and thus a higher Ga
470 content, apart from the late-stage high-REE dolomite carbonatite (CDD2-25A). The tightly
471 constrained nature and consistency of the Ga/Ge ratios for the majority of carbonatite
472 samples suggests that this ratio may reflect the mantle source.

473

474 H-C-O stable isotopes

475

476 Several groupings and trends in the C-O isotope data can be defined for the CRCC samples
477 (Table 5; Fig. 10). High-Sr calcite carbonatites form a group with a range in $\delta^{18}O$ of 7.5 to
478 8.6 ‰ and $\delta^{13}C$ of -4.2 to -4.0 ‰. This group exhibits a positive $\delta^{13}C$ shift (1) at almost
479 constant $\delta^{18}O$ from a theoretical uncontaminated mantle source composition. Seven
480 samples of dominantly dolomite carbonatite (with one sample of calcite carbonatite) define
481 a weak positive trend over the ranges in $\delta^{18}O$ of 8.3 to 12.6 ‰ and $\delta^{13}C$ of -3.4 to -2.2 ‰
482 (shift 2). A group of low-Sr dolomite carbonatite samples (with vuggy textures) have $\delta^{18}O$
483 values from 20.8 to 21.9‰, with a relatively narrow range in $\delta^{13}C$ of -4.3 to -3.6 ‰ (shift 3
484 from the primary carbonatite field). The clinopyroxenite samples define two groups, one
485 with $\delta^{18}O$ values from 11.1 to 11.3 ‰ and $\delta^{13}C$ from -5.6 to -5.4 ‰, and another group

with $\delta^{18}O$ from 9.7 to 11.2 ‰ and $\delta^{13}C$ from -4.4 to -3.9 ‰ that includes one amphibole-apatite phoscorite. One further clinopyroxenite sample contains calcite that has experienced a large shift in $\delta^{18}O$ compared to the signature of other clinopyroxenites ($\delta^{18}O$ = 21.4 ‰, $\delta^{13}C$ = -3.8 ‰). The results of $H_2O$-contents and stable H isotope analysis of fluid inclusion-hosted $H_2O$, as well as bulk carbonate C and O isotope compositions for ten carbonate samples from various carbonatites are presented in Table 6 and Fig. 11.

## Discussion

### Evolution of the Cummins Range carbonatites

Current evidence suggests that carbonatite magmas may have evolved from mantle-derived alkali-rich carbonated silicate magmas by some form of fractional crystallization or liquid immiscibility (e.g. Lee and Wylie 1998; Downes et al. 2005; Chakhmouradian and Zaitsev 2012). Alternatively, a small number of carbonatites probably were derived directly from the mantle by partial melting of metasomatised peridotite (e.g. Ray et al. 2013; Chakhmouradian and Zaitsev 2012). At Cummins Range, the association of the carbonatites with coeval clinopyroxenite suggests a genetic relationship between the two. No evidence for any form of liquid immiscibilty (e.g. conjugate silicate-carbonate or silicate-phosphate melts, or melt inclusion evidence of two immiscible liquids) involved in the evolution of the Cummins Range carbonatites has been discovered so far, however the operation of fractional crystallization processes is evident from the presence of apatite-

phlogopite-magnetite (± ilmenite ± pyrochlore) rich bands within the carbonatites, and cumulate textures in associated phoscorite and clinopyroxenite in parts of the CRCC. The fractionation of REE-poor magnetite, ilmenite, phlogopite and/or diopside, along with dolomite or calcite, is thought to have played a role in the derivation of the late-stage, high-REE dolomite carbonatite dykes at Cummins Range. However, this picture is complicated by the role of apatite in controlling the REE budget in these rocks. Bands of cumulate-textured apatite-amphibole-rich carbonatite are enriched in Zr, Nb, REEs, F, P and Na in comparison to associated calcite carbonatite (compare CDD2-21A and CDD2-27). The increased REE content in the cumulate rock could be related to higher apatite content, but Na-Zr-REE-bearing metasomatic–hydrothermal fluids have also altered these rocks, where zircon and amphiboles appear to overprint the primary fabric and calcite replaces monazite-(Ce) after apatite. One of the cumulate-textured apatite-amphibole phoscorite units (CDD1-22) also is hydrothermally mineralised, with minor fluorite replacing carbonate, and this is reflected in the relatively high Y, HREE and F content of this rock. Therefore, apart from one very low volume parisite-(Ce)-bearing dolomite carbonatite dyke (1), the primary magmatic carbonatites do not appear to have been greatly enriched in REEs by magmatic fractionation processes. Hydrothermal processes probably were of greater importance in enriching the high-REE dolomite carbonatite dyke (2) in LREEs (see below).

The HFSE chemistry of the Cummins Range carbonatites shows similarities to carbonatites from the Kola Alkaline Province in Russia (e.g. Zr/Hf and Zr/Nb ratios), but is notably different from post-orogenic carbonatites such as Eden Lake, Canada where the Zr/Nb ratio (24.5; Chakhmouradian et al. 2008) is much higher than the worldwide carbonatite average of 0.8 (Chakhmouradian 2006). In contrast to the low Zr and Hf content

of the Cummins Range carbonatites, the associated clinopyroxenite is extremely enriched in these elements (Fig. 3). Therefore, if the primary high-Sr calcite carbonatite was derived from a carbonated silicate parental magma, then the very low Nb, Ta, Zr and Hf content of the carbonatites could be a function of the fractionation of phases such as zirconolite. The relationship between the clinopyroxenite and the carbonatites will be explored in more detail in subsequent work.

Stable C and O isotope data for the high-Sr dolomite carbonatites and one high-REE dolomite carbonatite dyke exhibits a significant shift (2; Fig. 10) from the primary carbonatite field that could be indicative of either Rayleigh fractionation, an internal fluid/magma/mineral evolution with the crystallization and cooling of a $CO_2$-$H_2O$-bearing magma (see Deines 1989; Demény et al. 2004; Ray and Ramesh 1999, 2000, 2006), the direct assimilation of sedimentary carbonate (e.g. Santos and Clayton 1995), or addition of external carbon by infiltrating fluids (Demény et al. 1998). Rayleigh fractionation appears to be a more likely process in producing shift (2) than the assimilation of sedimentary carbonate given the geological setting of the CRCC, which has intruded the metamorphosed siliciclastic sediments of the Archean Olympio Formation and gneisses of the Paleoproterozoic Lamboo Complex (Andrew 1990). The dolomite carbonatite sample (CR7) that defines the furthest extent of this trend (2) in the CRCC data ($\delta^{18}O$ = 12.6 ‰, $\delta^{13}C$ = -2.2 ‰) is composed of turbid, microporous dolomite and contains minor quartz veining and weak REE mineralization associated with vugs. This suggests that the sample has been hydrothermally altered, and possibly it experienced a positive shift in $\delta^{18}O$ from its primary isotopic composition similar to other hydrothermally altered samples. The high-Sr dolomite carbonatites that fall along this trend (2) have relatively fractionated

554 LREE/HREE patterns ($La/Yb_{CN}$ ~ 96.5–352), along with depletions in the HREEs and Y in
555 comparison to the high-Sr calcite carbonatites and low-Sr dolomite carbonatites (Fig. 9).
556 This includes the dolomite carbonatite dyke (CDD1-37B; $\delta^{18}O$ = 9.1 ‰, $\delta^{13}C$ = -2.9 ‰)
557 associated with the high-REE apatite-monazite-(Ce) rock in CDD1.

558 In the high-REE dolomite carbonatite (CDD2-25), the pink calcite that replaces
559 primary apatite and associated monazite-(Ce) has higher $\delta^{18}O$ than groundmass dolomite.
560 This indicates a shift in $\delta^{18}O$ at relatively constant $\delta^{13}C$ that may have been produced by
561 postmagmatic isotope exchange with a water-rich carbonatitic fluid (cf. Zaitsev et al. 2002)
562 and there is evidence for the exsolution of an aqueous fluid phase indicated by the REE
563 geochemistry of this dyke (low Y/Ho ratio and Eu anomaly; cf. Buhn et al. 2001; Buhn
564 2008). The second high-REE dolomite carbonatite (CDD2-26) has a more extreme $\delta^{18}O$
565 value that suggests hydrothermal alteration similar to shift (3). Both of these dolomite
566 carbonatite dykes exhibit a positive shift in $\delta^{13}C$ (-3 to -3.3 ‰) in comparison to the group
567 of high-Sr calcite carbonatites with $\delta^{13}C$ ~ -4 ‰. This shift may have been produced by
568 Rayleigh fractionation processes as outlined above (shift 2), or by the addition of external
569 carbon in the form of dissolved $HCO_3^-$ or $CO_3^{2-}$ in the infiltrating fluid (Demény et al.
570 1998; Demény et al. 2004).

571 Stable hydrogen isotope compositions of water trapped in inclusions can provide
572 constraints on the origin of fluids as the δD values can significantly differ between primary
573 magmatic water and crustal solutions (Sheppard 1986). The present δD dataset ranges from
574 –54 to –34 ‰ (Fig. 11, Table 6), which is similar to the upper limit of the δD range
575 obtained for the Speewah complex ~330 km NNE of the CRCC (Fig. 1; Czuppon et al.
576 2014). Within this δD range no systematic change was found with the $H_2O$ content (i.e., the

amount of inclusion-hosted water; Fig. 11a) of the carbonate samples, thus the degassing and/or mixing processes assumed for the Speewah complex did not affect the Cummins Range rocks. Both the $\delta^{13}C$ and $\delta^{18}O$ data vary independently from the δD values (Fig. 11b, c) suggesting that the evolution of the carbonatite system was not related to mixing of fluids of different origins.

## Hydrothermal processes and REE mineralization

The highest grade REE mineralization discovered so far beneath the oxidised zone within the CRCC is the unusual apatite-monazite-(Ce) rock intersected in drill hole CDD1 over the interval 261.85–275.2 m (Figs 6, 7). The limited intersection of this REE-rich zone and the broken nature of the drill core does not allow for a comprehensive interpretation of its origin. In the CRCC, those intervals that show the complex intergrowth of fine, elongated monazite-(Ce) crystals in apatite are cut by veins of talc-amphibole that appears to preferentially replace apatite (Fig. 7). Associated foliated rocks in which monazite-(Ce) crystals occur in a talc-amphibole matrix may have developed from more apatite-rich rocks in which the apatite has been replaced by talc during metasomatism/hydrothermal alteration (Fig. 7). Several lines of evidence suggest a hydrothermal origin for the high-REE apatite-monazite-(Ce) rock. Firstly, the texture of the apatite vein adjacent to the apatite-monazite-(Ce) zone illustrated in Fig. 6 indicates hydrothermal growth. In addition, the composition of apatite from the apatite-monazite-(Ce) rock is quite distinct from that of magmatic apatite in associated carbonatites in terms of Sr and REE content (Fig. 8). High-Sr

hydrothermal apatite with some textural and compositional similarities to this occurs in hydrothermal phosphate vein-type ores from the southern Central Iberian Zone, Spain (Vindel et al. 2014). De Toledo et al. (2004) also described high-Sr hydrothermal apatites from the Catalao I alkaline-carbonatite complex in Brazil. Positive Eu anomalies in the REE-enriched cores of some zoned apatite crystals in the high-REE apatite-monazite-(Ce) rock suggest crystallization from a Eu-enriched fluid under reducing conditions (cf. Vindel et al. 2014). The very large enrichment in the LREEs evident in the chondrite-normalised REE pattern of the apatite-monazite-(Ce) rock also is consistent with hydrothermal mineralization (Fig. 9a; cf. Ngwenya 1994; Ruberti et al. 2008). The apatite-monazite-(Ce) rock exhibits shifts to higher $\delta^{18}O$ in comparison to an associated dolomite carbonatite dyke (Fig. 10). Texturally, the dolomite in this apatite-monazite-(Ce) rock appears to be associated with talc-amphibole-pyrrhotite veining that crosscuts the apatite-monazite-(Ce) fabric and this shift in $\delta^{18}O$ probably is related to hydrothermal alteration. A factor controlling the occurrence of this high-grade apatite-monazite-(Ce) rock appears to have been the initial presence of an apatite-rich lithology within the shear zone that was subject to subsequent hydrothermal mineralization, where monazite-(Ce) precipitated from REE-rich fluids, and partially replaced and overprinted apatite. The shear zone was the conduit for hydrothermal fluid flow probably contemporaneously with carbonatite emplacement. The timing of this monazite-(Ce) mineralization is presently the subject of further geochronological studies.

Hydrothermal alteration at decreasing temperature probably produced the significant shift from the primary carbonatite field seen particularly in the low-Sr, weakly mineralised, dolomite carbonatites (Fig. 10). The widespread hydrothermal dolomitization of

carbonatites within the CRCC and the occurrence of associated talc-rich zones within shear zones suggests some similarities to a number of hydrothermal talc deposits, e.g. Ruby Mountains, Montana, USA (Anderson et al. 1990; Brady et al. 1998); Puebla de Lillo, Cantabrian zone, Variscan belt of Iberia, Northern Spain (Tornos and Spiro 2000); and Göpfersgrün, Fichtelgebirge, Germany (Hecht et al. 1999). The talc may have precipitated from Mg and Si-rich hydrothermal fluids at temperatures of approximately 250–400˚C (cf. Hecht et al. 1999). An indication of retrograde hydration is the widespread replacement of diopside by actinolite (uralitization) in the clinopyroxenite. The source of Mg for the formation of talc and dolomite is uncertain but may be the associated clinopyroxenite.

It appears that the most important episode of REE mineralization in the Cummins Range carbonatites probably was associated with the late magmatic–hydrothermal phase of carbonatite emplacement, where REEs were mobilised from primary magmatic carbonates (Sr-bearing calcite) and apatite to produce monazite-(Ce) and the REE-fluorocarbonates, parisite-(Ce) and synchysite-(Ce) (cf. Wall and Mariano 1996; Wall and Zaitsev 2004; Chakhmouradian and Zaitsev 2012). A recent review of the transport and deposition of REEs by hydrothermal fluids (Williams-Jones et al. 2012) suggested that a high chloride activity was an important feature of the fluids involved. Chloride species are thought to transport the REEs in most hydrothermal systems (Williams-Jones et al. 2012). At Cummins Range, a possible mechanism for the deposition of the parisite-(Ce) and synchysite-(Ce) could have been:

$REECl^{2+} + HF + 2HCO_3^- + Ca^{2+} = REECa(CO_3)_2F + 3H^+ + Cl^-$ (cf. Williams-Jones et al. 2012).

644 The development of vugs in the low-Sr dolomite carbonatite indicates that some
645 dolomite (or calcite) was dissolved probably through reaction with hydrothermal fluids.
646 The following reaction involving the dolomite carbonatite may have increased the $HCO_3^-$
647 activity and raised the pH of the fluids:

648 $$2H^+ + CaMg(CO_3)_2 = Ca^{2+} + Mg^{2+} + 2HCO_3^-,$$

649 resulting in the precipitation of parisite-(Ce) and synchysite-(Ce) in solution cavities (cf.
650 Williams-Jones et al. 2012). Reaction with host carbonatite wall rocks appears to have been
651 a valid mechanism for the precipitation of REE-fluorocarbonates. Monazite-(Ce) most
652 commonly occurs rimming or replacing primary apatite, whereas the REE-fluorocarbonates
653 are generally restricted to a carbonate host. The replacement of apatite by monazite-(Ce) is
654 a common relationship in hydrothermal settings (see Wall and Mariano 1996; Smith et al.
655 1999), and apatite dissolution and monazite-(Ce) precipitation may have proceeded as
656 follows:

657 $$Ca_5(PO_4)_3F + 4H^+ + REECl^{2+} = REEPO_4 + 5Ca^{2+} + 2H_2PO_4^- + F^- + Cl^-$$

658

659 Relationship between carbonatites and associated clinopyroxenite and phoscorite

660

661 The H-C-O stable isotope data provide some insight into the relationship between the
662 carbonatites and associated clinopyroxenite and phoscorite in the CRCC. Cummins Range
663 exhibits similarities in stable isotope patterns to some of the carbonatite-phoscorite
664 complexes from the Kola Alkaline Province (Demény et al. 2004). Two samples of

clinopyroxenite and one of an amphibole-apatite phoscorite have $\delta^{13}C$ values of ~ -4 ‰ similar to associated high-Sr calcite carbonatite (Fig. 10). The slight positive shift in $\delta^{18}O$ for these samples is consistent with carbonate-silicate isotope exchange at decreasing temperatures (cf. Deines 1989; Demény et al. 2004). One clinopyroxenite sample (CDD2-24) shows a more extreme shift in $\delta^{18}O$ that suggests that it might have been affected by hydrothermal alteration. Of particular interest are the two clinopyroxenite samples (CDD2-11, CDD2-14) that have $\delta^{13}C$ values (-5.62 to -5.38 ‰) more within the range of primary mantle carbonate and similar to values for the Mt Weld carbonatite in Western Australia. The shift in $\delta^{18}O$ for these samples, to place them outside the range for primary igneous carbonate, also could be related to carbonate-silicate isotope exchange at decreasing temperatures (cf. Deines 1989; Demény et al. 2004). These samples do not show the shift in $\delta^{13}C$ that distinguishes the high-Sr calcite carbonatites and some clinopyroxenite and phoscorite samples (shift 1). This could mean that they are derived from a separate mantle source that has been unaffected by source contamination.

The relatively high δD values from the Cummins Range carbonatites indicate that the fluid associated with carbonate formation contained a significant amount of crustal component in accordance with the elevated $\delta^{13}C$ values. The normal magmatic $\delta^{18}O$ values (between 6 and 10 ‰) of some of the carbonates at higher-than-mantle C isotopic compositions, however, suggest that the O isotope compositions in these samples were buffered by a magmatic silicate reservoir at high temperature. These observations collectively indicate that the carbonated silicate magma interacted with crustal fluids at depth, and this interaction shifted the H and C isotope compositions due to the relatively high proportion of H and C in the fluid relative to the magma. In contrast to H and C, the O

688 isotope compositions were buffered by the silicate magma from which the carbonate melt
689 and associated fluids were separated.

690

691 Nature and evolution of mantle source regions

692

693 From initial work on a limited range of samples, the Cummins Range carbonatite has
694 quite primitive Sr-Nd isotope compositions suggesting that it is derived from an OIB-type
695 source within the depleted convecting mantle ($^{87}Sr/^{86}Sr$ = 0.7028–0.7032; $\varepsilon$ Nd = 1.6–2.4;
696 Sun et al. 1986). This source is quite distinct from the radiogenic, enriched mantle sources
697 of the Mesoproterozoic Argyle lamproite (Jaques et al. 1989b) and the Miocene lamproites
698 of the West Kimberley province (McCulloch et al. 1983; Fraser et al. 1985). The high
699 starting $\delta^{13}C$ value of around -4 ‰ for the source of the Cummins Range carbonatites
700 therefore could mean metasomatism of the mantle source region by $CO_2$ released by a
701 subducted slab (Ray and Ramesh 1999; Zaitsev et al. 2002), or perhaps the removal of a
702 $^{13}C$-depleted component within the mantle via isotope fractionation processes (Deines
703 2002).

704 Several authors have proposed that a period of NW-dipping subduction beneath the
705 Kimberley Craton occurred during the Paleoproterozoic, before the eventual collision and
706 amalgamation of the craton with the remainder of the North Australian Craton at
707 approximately 1820 Ma (Myers et al. 1996; Tyler et al. 1999; Griffin et al. 2000). This was
708 the last period during which subduction-related processes would have influenced the mantle
709 beneath the East Kimberley. The ~1800 Ma Hart Dolerite, a widespread series of tholeiitic

basaltic and related granophyre intrusions centered in the SE of the Kimberley Craton (Fig. 1), is inferred to have been sourced from subduction-modified mantle beneath the Kimberley Craton, and was closely related to plate reorganization in late Paleoproterozoic Australia (Sheppard et al. 2013). Other evidence of plate-margin processes are provided by C isotopic and mineral inclusion studies of eclogitic diamonds from the Argyle lamproite that suggest that they probably formed in subducted oceanic crust that was accreted to the base of the lithosphere in the Proterozoic (Jaques et al. 1989a). Schulze et al. (2013) interpreted an association of light $\delta^{13}C$ in Argyle eclogitic diamonds with high $\delta^{18}O$ values of their garnet and coesite silicate inclusions to indicate a subduction origin. A recent study of the noble gas and C isotopic composition of eclogitic diamonds from Argyle suggests that mixing had occurred between a subducted atmospheric and crustal component and mantle noble gases in their formation (Honda et al. 2012).

Further Sr-Nd isotopic analysis is required to examine the observed variation in $\delta^{13}C$ in some clinopyroxenite samples from the CRCC and confirm that they are derived from a separate mantle source unaffected by subduction-related $CO_2$ metasomatism or the removal of a $^{13}C$-depleted component within the mantle.

There are several processes that could explain the high δD values of the Cummins Range carbonatites. Degassing of $H_2$ from the mantle source would leave the residual fluid enriched in deuterium, so the source may acquire a high δD signature (e.g. see Demény et al. 2012). However, this process would not produce high $\delta^{13}C$. Alternatively, interaction with crustal fluids at crustal levels may have taken place, where the emplacement of a carbonated silicate magma may have induced a convective flow in the fluids surrounding the complex. If these fluids had a high-δD signature and the magma interacted with these

733 fluids, the magma, and later the segregated carbonate melt would have a high-δD fluid
734 component too. Mixing of magmatic fluids and waters circulating in the surrounding
735 country rocks may well have produced a fluid with δD around -40 ‰ as observed. This is
736 possible, as we see appropriate fluid compositions regionally, for example at Speewah
737 (Czuppon et al. 2014), but in this case the C and O isotope compositions should show at
738 least a slight change with δD. No such correlation is evident in Fig. 11. The preservation of
739 primitive Sr and Nd isotope compositions in the Cummins Range carbonatite would also
740 argue against significant exchange with crustal fluids in this way. Finally, the subduction
741 and devolatilization of oceanic crust may have provided D-enriched fluids that could, for
742 example, have metasomatised the mantle wedge (e.g. Giggenbach 1992). The release of
743 $CO_2$ and $H_2O$ from a subducting slab would produce high δD and $\delta^{13}C$ in the
744 metasomatised mantle, but the O isotope composition would be buffered by the silicate
745 mass. $CO_2$-$H_2O$ fluids without melt may not contain significant amounts of Sr and Nd, so
746 the magma's Sr-Nd isotope compositions would remain intact. Therefore it appears that the
747 δD signature of the Cummins Range carbonatites could be a further indication subduction-
748 related metasomatism of the mantle source.

749

## 750 Summary

751

752 The CRCC was emplaced at the junction of the Paleoproterozoic Halls Creek and King
753 Leopold paleo-orogenic belts at the margin of the Kimberley Craton probably during a
754 phase of Neoproterozoic extension. Trace-element geochemistry suggests that the
755 carbonatites have affinities to rift-related carbonatites (cf. Chakhmouradian 2009) and

generally are not greatly enriched in the REEs (Fig. 9a). The Cummins Range carbonatites follow an intrusive sequence where early calcite carbonatite, possibly derived from a carbonated silicate parental magma by fractional crystallization, has been intruded by late-stage dolomite carbonatites with higher REE content (Fig. 12; cf. Wall and Mariano 1996). The shift in C-O stable isotope data from the primary carbonatite field for the high-Sr dolomite carbonatites and a high-REE dolomite carbonatite is consistent with a process of Rayleigh fractionation with magma crystallization and cooling. These dolomite carbonatites may have been derived from the calcite carbonatites through the fractionation of phases such as dolomite and apatite. Hydrothermal and metasomatic processes, probably involving fluids exsolved from the carbonatites, produced widespread dolomitization of the carbonatites and high-grade REE mineralization in a late-stage dolomite carbonatite dyke and in shear zone-hosted apatite-monazite-(Ce) rocks. The relatively high δD values (–54 to –34 ‰) of $H_2O$ derived from carbonatites from the CRCC indicate that the fluids associated with carbonate formation contained a significant amount of crustal component in accordance with the elevated $\delta^{13}C$ values (~ -4 ‰). The high δD and $\delta^{13}C$ signature of the carbonatites may have been produced by $CO_2$-$H_2O$ metasomatism of the mantle source during Paleoproterozoic subduction beneath the eastern margin of the Kimberley Craton.

## Acknowledgements

We would like to thank Bernie Kirkpatrick from Navigator Resources and Geoff Collis from Kimberley Rare Earths for providing samples and geological data from the CRCC, as well as company illustrations and images. Geochemical analyses were funded in part by the Geological

779 Survey of Western Australia, the Hungarian Academy of Sciences and the Western Australian
780 Museum. We thank Liz Webber and Bill Pappas for the geochemical analyses undertaken at
781 Geoscience Australia and Jeremy Wykes for the LA-ICP-MS analyses done at ANU. James Tolley
782 (ANU) kindly provided a digital version of the simplified geological map. Dr Lena Hancock from
783 the GSWA provided Hylogger data and helped with discussions of the Cummins Range geology.
784 The staff of the GSWA core library provided access to and samples from the Cummins Range drill
785 core. Prof. A.E. Williams-Jones and an anonymous reviewer provided very helpful detailed reviews
786 of an earlier version of this manuscript. Dr Ben Grguric gave helpful guidance in the interpretation
787 of sulfide and replacement textures.

788

## 789 References

790

791 Anderson DL, Mogk DW, Childs JF (1990) Petrogenesis and timing of talc formation in
792 the Ruby Range, southwestern Montana. Economic Geology 85:585–600.

793 Andrew R (1990) Cummins Range Carbonatite. In: Hughes FE (ed) Geology of the Mineral
794 Deposits of Australia and Papua New Guinea. AusIMM, Melbourne, pp 711-713

795 Belousova EA, Griffin WL, O'Reilly SY, Fisher N (2002) Igneous zircon: trace element
796 composition as an indicator of source rock type. Contrib Mineral Petrol 143:602–622.
797 doi: 10.1007/s00410-002-0364-7

798 Brady JB, Cheney JT, Rhodes AL, Vasquez A, Green C, Duvall M, Kogut A, Kaufman L,
799 Kovaric D (1998) Isotope geochemistry of Proterozoic talc occurrences in Archean
800 marbles of the Ruby Mountains, southwest Montana, USA. Geol Mat Res 1:1–41.

801 Bühn B, Wall F, Le Bas MJ (2001) Rare-earth element systematics of carbonatitic
802 fluorapatites, and their significance for carbonatite magma evolution. Contrib Mineral
803 Petrol 141(5):572–591

804 Bühn B (2008) The role of the volatile phase for REE and Y fractionation in low-silica
805 carbonate magmas: implications from natural carbonatites, Namibia. Mineral Petrol
806 92(3-4):453–470

807 Cawood PA, Korsch RJ (2008) Assembling Australia: Proterozoic building of a continent.
808 Precamb Res 166:1–38

809 Chakhmouradian AR (2009) The geochemistry of carbonatites revisited: Two major types
810 of continental carbonatites and their trace-element signatures. EGU General
811 Assembly 2009, held 19-24 April, 2009 in Vienna, Austria http://meetings copernicus
812 org/egu2009, p 10806 11:10806

813 Chakhmouradian AR, Böhm CO, Demény A, Reguir EP, Hegner E, Creaser RA, Halden
814 NM, Yang P (2009) "Kimberlite" from Wekusko Lake, Manitoba: Actually a
815 diamond-indicator-bearing dolomite carbonatite. Lithos 112:347–357. doi:
816 10.1016/j.lithos.2009.03.039

817 Chakhmouradian AR, Mumin A, Demény A, Elliott B (2008) Postorogenic carbonatites at
818 Eden Lake, Trans-Hudson Orogen (northern Manitoba, Canada): geological setting,
819 mineralogy and geochemistry. Lithos 103:503–526

820 Chakhmouradian AR, Zaitsev AN (2012) Rare Earth Mineralization in Igneous Rocks:
821 Sources and Processes. Elements 8(5):347–353

822 Czuppon Gy, Ramsay RR, Özgenc I, Demény A, Gwalani LG, Rogers K, Eves A, Papp L,
823 Palcsu L, Berkesi M, Downes PJ (2014) Stable (H, O, C) and noble-gas (He and Ar)
824 isotopic compositions from calcite and fluorite in the Speewah Dome, Kimberley
825 Region, Western Australia: Implications for the conditions of crystallization and
826 evidence for the influence of crustal-fluid mixing. Mineral Petrol doi:
827 10.1007/s00710-014-0333-7.

828 Demény A (1995) H isotope fractionation due to hydrogen-zinc reactions and its
829 implications on D/H analysis of water samples. Chem Geol 121:19–25

830 Demény A, Ahijado A, Casillas R, Vennemann TW (1998) Crustal contamination and
831 fluid/rock interaction in the carbonatites of Fuerteventura (Canary Islands, Spain): a
832 C, O, H isotope study. Lithos 44(3-4):101–115

833 Demény A, Sitnikova MA, Karchevsky PI (2004) Stable C and O isotope compositions of
834 carbonatite complexes of the Kola alkaline province: phoscorite-carbonatite
835 relationships and source compositions. In: Wall F, Zaitsev AN (eds) Phoscorites and
836 Carbonatites from Mantle to Mine. Mineralogical Society Series 10, Mineralogical
837 Society, London, pp 407–431

838 Demény A, Siklósy Z (2008) Combination of off-line preparation and continuous flow
839 mass spectrometry: D/H analyses of inclusion waters. Rapid Comm Mass Spect
840 22:1329-1334

841 Demény A, Harangi S, Vennemann TW, Casillas R, Horváth P, Milton AJ, Mason PRD,
842 Ulianov A (2012) Amphiboles as indicators of mantle source contamination:
843 Combined evaluation of stable H and O isotope compositions and trace element

ratios. Lithos 152:141–156. doi:10.1016/j.lithos.2012.07.001

De Toledo M, Lenharo S, Ferrari V, Fontan F, De Parseval P, Leroy G (2004) The compositional evolution of apatite in the weathering profile of the Catalão I alkaline-carbonatitic complex, Goiás, Brazil. Can Mineral 42:1139–1158.

Downes H, Balaganskaya E, Beard AD, Liferovich RP, Demaiffe D (2005) Petrogenetic processes in the ultramafic, alkaline and carbonatitic magmatism in the Kola Alkaline Province: A review. Lithos 85:48–75. doi: 10.1016/j.lithos.2005.03.020

Eggins SM, Woodhead JD, Kinsley LPJ, Mortimer GE, Sylvester P, McCulloch MT, Hergt JM, Handler MR (1997) A simple method for the precise determination of ≥ 40 trace elements in geological samples by ICPMS using enriched isotope internal standardisation. Chem Geol 134:311–326. doi: http://dx.doi.org/10.1016/S0009-2541(96)00100-3

Fraser KJ, Hawkesworth CJ, Erlank AJ, Mitchell RH, Scott-Smith BH (1985) Sr, Nd and Pb isotope and minor element geochemistry of lamproites and kimberlites. Earth Planet Sci Lett 76:57–70.

Geological Survey of Western Australia (2011) Investment opportunities–Rare Earths. http://www.hastingsraremetals.com/wp-content/uploads/2012/07/2011-10-03-7_wa-mines-dept-rare-earth-october-2011.pdf. Accessed 20 December 2013

Giggenbach WF (1992) Isotopic shifts in waters from geothermal and volcanic systems along convergent plate boundaries and their origin. Earth Planet Sci Lett 113:495–510

865 Graham S, Lambert D, Shee S (2004) The petrogenesis of carbonatite, melnoite and
866 kimberlite from the Eastern Goldfields Province, Yilgarn Craton. Lithos 76:519–533

867 Griffin TJ, Page RW, Sheppard S, Tyler IM (2000) Tectonic implications of
868 Palaeoproterozoic post-collisional, high-K felsic igneous rocks from the Kimberley
869 region of northwestern Australia. Precamb Res 101:1–23

870 Hassan LY (2000) Mineral occurrences and exploration potential of the East Kimberley.
871 Geological Survey of Western Australia Report 74, Department of Minerals and
872 Energy, Perth, 60 pp

873 Hecht L, Freiberger R, Gilg HA, Grundmann G, Kostitsyn YA (1999) Rare earth element
874 and isotope (C, O, Sr) characteristics of hydrothermal carbonates: genetic
875 implications for dolomite-hosted talc mineralization at Göpfersgrün (Fichtelgebirge,
876 Germany). Chem Geol 155:115–130.

877 Honda M, Phillips D, Kendrick MA, Gagan MK, Taylor WR (2012) Noble gas and carbon
878 isotope ratios in Argyle diamonds, Western Australia: Evidence for a deeply
879 subducted volatile component. Australian J Earth Sci 59(8):1135-1142

880 Jaques AL, Lewis JD, Smith CB (1986) The kimberlites and lamproites of Western
881 Australia. Geological Survey of Western Australia Bulletin 132, 268 pp

882 Jaques AL, Hall AE, Sheraton JV, Smith CB, Sun SS, Drew R, Foudoulis C, Ellingsen K
883 (1989a) Composition of crystalline inclusions and C-isotopic composition of Argyle
884 and Ellendale diamonds. In: Ross J et al. (eds) Kimberlites and Related Rocks: Their

885 Crust/Mantle Setting, Diamonds and Diamond Exploration. Geol Soc Australia Spec
886 Publ 14, vol. 2, pp 966–989

887 Jaques AL, Sun SS, Chappell BW (1989b) Geochemistry of the Argyle (AK1) lamproite
888 pipe, Western Australia. In: Ross J et al. (eds) Kimberlites and Related Rocks: Their
889 Composition, Occurrence, Origin and Emplacement. Geol Soc Australia Spec Publ
890 14, vol. 1, pp 170–188

891 Jaques AL, Milligan (2004) Patterns and controls on the distribution of diamondiferous
892 intrusions in Australia. Lithos 77(1-4):783-802

893 Jenner FE, O'Neill HS-C (2012) Major and trace analysis of basaltic glasses by laser-
894 ablation ICP-MS. Geochem. Geophys. Geosyst. 13, Q03003,
895 doi:10.1029/2011GC003890.

896 Johnson SP (2013) The birth of supercontinents and the Proterozoic assembly of Western
897 Australia. Geological Survey of Western Australia, Perth, 78pp

898 Keller J, Hoefs J (1995) Stable isotope characteristics of recent natrocarbonatites from
899 Oldoinyo Lengai. In: Bell K, Keller J (eds) Carbonatite volcanism: Oldoinyo Lengai
900 and the petrogenesis of natrocarbonatites. Springer Verlag, Berlin, pp 113–123

901 Kimberley Rare Earths (2012) Annual report to shareholders. Perth, Western Australia, pp
902 1–54. http://anovametals.com.au/wp-
903 content/uploads/2012/11/206_KRE_2012_Annual_Report_to_Shareholders_Final.pd
904 f. Accessed 20 December 2013

905 Krasnova NI, Petrov TG, Balaganskaya EG, Garcia D, Moutte J, Zaitsev AN, Wall F
906 (2004) Introduction to phoscorites: occurrence, composition, nomenclature and
907 petrogenesis. In: Wall F and Zaitsev AN (eds), Phoscorites and Carbonatites from
908 Mantle to Mine: the key example of the Kola Alkaline Province. Mineralogical
909 Society Series 10, Mineralogical Society, London, pp 45–74

910 Lee W, Wyllie PJ (1998) Processes of crustal carbonatite formation by liquid immiscibility
911 and differentiation, elucidated by model systems. J Petrol 39:2005–2013

912 Luguet A, Jaques AL, Pearson DG, Smith CB, Bulanova GP, Roffey SL, Rayner MJ,
913 Lorand JP (2009) An integrated petrological, geochemical and Re–Os isotope study
914 of peridotite xenoliths from the Argyle lamproite, Western Australia and implications
915 for cratonic diamond occurrences. Lithos 112:1096-1108

916 McCulloch MT, Jaques AL, Nelson D, Lewis JD (1983) Nd and Sr isotopes in kimberlites
917 and lamproites from Western Australia: an enriched mantle origin. Nature 302: 400–
918 403

919 Myers JS, Shaw RD, Tyler IM (1996) Tectonic evolution of Proterozoic Australia.
920 Tectonics 15:1431–1446

921 Nelson DR, Chivas AR, Chappell BW, McCulloch MT (1988) Geochemical and isotopic
922 systematics in carbonatites and implications for the evolution of ocean-island sources.
923 Geochim Cosmochim Acta 52(1):1–18

924 Ngwenya BT (1994) Hydrothermal rare earth mineralisation in carbonatites of the Tundulu
925 complex, Malawi: Processes at the fluid/rock interface. Geochimica Cosmochim Acta
926 58(9):2061–2072

927 Norrish K, Chappell BW (1977) X-ray fluorescence spectrometry. In: Zussman J (ed)
928 Physical methods in determinative mineralogy, 2nd edn. Academic Press, London, pp
929 201–272.

930 Norrish K, Hutton JT (1969) An accurate X-ray spectrographic method for the analysis of a
931 wide range of geological samples. Geochim Cosmochim Acta 33(4):431–453

932 Palme H, O'Neill HStC (2005) Cosmochemical estimates of mantle composition. In: RW
933 Carlson (ed) The Mantle and Core, Vol. 2 Treatise on Geochemistry. Elsevier–
934 Pergamon, Oxford, pp 1–38

935 Paton, C, Hellstrom, J, Bence, P, Woodhead, J, Hergt, J (2011) Iolite: Freeware for the
936 visualisation and processing of mass spectrometric data. J. Anal. At. Spectrom.
937 26:2508-2518

938 Pidgeon RT, Smith CB, Fanning CM (1986) The ages of kimberlite and lamproite
939 emplacement in Western Australia. In: 4th International Kimberlite Conference,
940 Perth, 1986, Geol. Soc. Aust. Abstr. 16, pp 136-138

941 Pyke J (2000) Minerals laboratory staff develops new ICP-MS preparation method. Aust.
942 Geol. Survey Org. Res. Newslett. 33:12–14

943 Ray J, Ramesh R (1999) Evolution of carbonatite complexes of the Deccan flood basalt
944 province: stable carbon and oxygen isotopic constraints. J Geophys Res 104:29471–
945 29483

946 Ray J, Ramesh R (2000) Rayleigh fractionation of stable isotopes from a multicomponent
947 source. Geochim Cosmochim Acta 64:299–306

948 Ray JS, Ramesh R (2006) Stable Carbon and Oxygen Isotopic Compositions of Indian
949 Carbonatites. Internat Geol Rev 48:17–45. doi: 10.2747/0020-6814.48.1.17

950 Ray JS, Pande K, Bhutani R, Shukla AD, Rai VK, Kumar A, Awasthi N, Smitha RS, Panda
951 DK (2013) Age and geochemistry of the Newania dolomite carbonatites, India:
952 implications for the source of primary carbonatite magma. Contrib Mineral Petrol
953 166:1613–1632. doi: 10.1007/s00410-013-0945-7

954 Richards MN (1984) Annual report for 1983 on exploration licence 80/113, Cummins
955 Range, Mt. Bannerman, SE52-13, Western Australia. CRA Exploration Pty. Ltd.
956 Report to West Australian Department of Mines and Petroleum, A14632, CRAE Ref.
957 No. 12981, 40 pp

958 Richards MN (1985) Annual report for 1984 on exploration licence 80/113, Cummins
959 Range, Mt. Bannerman, SE52-13, Western Australia, Volume 1. CRA Exploration
960 Pty. Ltd. Report to West Australian Department of Mines and Petroleum, A16631,
961 CRAE Ref. No. 13612, 20 pp

962 Ruberti E, Enrich GER, Gomes CB, Comin-Chiaramonti P (2008) Hydrothermal REE
963 fluorocarbonate mineralization at Barra do Itapirapua, a multiple stockwork
964 carbonatite, southern Brazil. Can Mineral 46(4):901–914

965 Sanders TS (1999) Mineralization of the Halls Creek Orogen, east Kimberley region,
966 Western Australia. Geological Survey of Western Australia Report 66, Department of
967 Minerals and Energy, Perth, 44 pp

968 Santos R, Clayton RN (1995) Variations of oxygen and carbon isotopes in carbonatites: a

969 study of Brazilian alkaline complexes. Geochim Cosmochim Acta 59:1339–1352.

970 Schulze D, Harte B, Page FZ, Valley JW, Channer DMDeR, Jaques AL (2013)
971 Anticorrelation between low $\delta^{13}C$ of eclogitic diamonds and high $\delta^{18}O$ of their coesite
972 and garnet inclusions requires a subduction origin. Geology 41:455–458

973 Shapiro LM, Brannock WW (1962) Rapid analysis of silicate, carbonate and phosphate
974 rocks. US Geological Survey Bulletin 1144-A. US Government Printing Office.

975 Sheppard S (1986) Characterization and isotopic variations in natural waters. In: Valley
976 JW, Taylor Jr HP, O'Neil JR (eds) Reviews in Mineralogy 16, Stable isotopes in high
977 temperature geological processes. Mineral Soc Amer, pp 165-184

978 Sheppard S, Page RW, Griffin TJ, Rasmussen B, Fletcher IR, Tyler IM, Kirkland CL,
979 Wingate MTD, Hollis JA, Thorne AM (2012) Geochronological and isotopic
980 constraints on the tectonic setting of the c. 1800 Ma Hart Dolerite and the Kimberley
981 and Speewah Basins, Northern Western Australia. Geological Survey of Western
982 Australia Record 2012/7, 28pp

983 Spötl C, Vennemann TW (2003) Continuous-flow IRMS analysis of carbonate minerals.
984 Rapid Commun Mass Spectrom 17:1004-1006

985 Sun S-S, Jaques AL, McCulloch MT (1986) Isotopic evolution of the Kimberley Block,
986 Western Australia. In: 4th International Kimberlite Conference, Perth, 1986, Geol.
987 Soc. Aust. Abstr. 16, pp 346-348

988 Taylor Jr HP, Frechen J, Degens ET (1967) Oxygen and carbon isotope studies of
989 carbonatites from the Laacher See District, West Germany and the Alno District,
990 Sweden. Geochim Cosmochim Acta 31:407–430

991 Tornos F, Spiro BF (2000) The geology and isotope geochemistry of the talc deposits of
992 Puebla de Lillo (Cantabrian Zone, Northern Spain). Economic Geology 95:1277–
993 1296.

994 Tyler IM, Page RW, Griffin TJ (1999) Depositional age and provenance of the Marboo
995 Formation from SHRIMP U–Pb zircon geochronology: implications for the early
996 Palaeoproterozoic tectonic evolution of the Kimberley region, Western Australia.
997 Precamb Res 95:225–243

998 Wall F, Mariano AN (1996) Rare earth minerals in carbonatites: a discussion centered on
999 the Kangankunde carbonatite, Malawi. In: Jones AP, Wall F, Williams CT (eds) Rare
1000 Earth Minerals: Chemistry, Origin and Ore Deposits. Mineralogical Society Series 7,
1001 Mineralogical Society, London, pp 193-225

1002 Wall F, Zaitsev AN (2004) Rare earth minerals in Kola carbonatites. In: Wall F, Zaitsev
1003 AN (eds) Phoscorites and Carbonatites from Mantle to Mine: The Key Example of
1004 the Kola Alkaline Province. Mineralogical Society Series 10, Mineralogical Society,
1005 London, pp 341-373

1006 Williams-Jones AE, Migdisov AA, Samson IM (2012) Hydrothermal Mobilisation of the
1007 Rare Earth Elements - a Tale of "Ceria" and "Yttria". Elements 8(5): 355-360

1008 Zaitsev AN, Demény A, Sindern S, Wall F (2002) Burbankite group minerals and their

alteration in rare earth carbonatites--source of elements and fluids (evidence from CO and Sr-Nd isotopic data). Lithos 62:15–33

# Appendix 1: Supplementary data

Exploration whole-rock geochemistry

The graphic drill logs of drill holes CDD1 (Fig. 3) and CDD2 (red circles indicate the positions of late-stage, high-REE dolomite carbonatite dykes) were constructed using historical exploration whole-rock geochemical analyses undertaken in 1984 by Pilbara Laboratories in Perth, on behalf of CRA Exploration (Richards, 1985). These partial analyses were carried out by inductively-coupled plasma emission spectroscopy (ICP). Full details of the analytical procedures are described by Richards (1985). This report is available for download from the Western Australian Department of Mines and Petroleum website (http://www.dmp.wa.gov.au/launch/wamex/). The full dataset for drill holes CDD1 and CDD2 is presented here. A plan illustrating a possible structural control on the orientation of the oxidised zone REE orebody in the CRCC is included (courtesy of Kimberley Rare Earths).

**Figure Captions**

**Fig. 1** Geological map showing the location of the Cummins Range Carbonatite Complex, Kimberley region, Western Australia (1:2500000 Geological Survey of Western Australia 2014, extracted from GeoVIEW.WA on 05/06/2014. Perth, Western Australia: Department of Mines and Petroleum.)

**Fig. 2** Geological map of the Cummins Range Carbonatite Complex (1:5000). Drill holes CDD001, NRC035, NRC058: azimuth 180˚ (mag.), inclination 60˚. CDD002: azimuth 270˚ (mag.), inclination 60˚. Geology modified after Richards (1985) and Andrew (1990) and based on company drilling. Only the locations of drill holes sampled for use in this study are shown.

**Fig. 3** Graphic log of drill hole CDD1. Red circles indicate the position of high-REE apatite-monazite-(Ce) rock associated with dolomite carbonatite dykes within a shear zone.

**Fig. 4 a** Pink high-Sr calcite (cc) carbonatite containing a zircon megacryst (zrc) in an apatite (ap)-amphibole-phlogopite-pyrochlore lamina, associated with magnetite (mt) and dolomite (dol) (CDD1 323.9 m). **b** Calcite carbonatite containing large crystals of magnetite, as well as amphibole (amp) and apatite (CDD2-4, 88.7 m). **c** High-Sr calcite carbonatite containing apatite, phlogopite (phl) and magnetite overprinted by metasomatic amphibole crystals (CDD2-21, 399.95 m). **d** Strongly foliated dolomite carbonatite containing a composite zircon-dolomite porphyroblast (py – pyrite; CR5, CDD1 204.35 m).

**Fig. 5 a** Grey, late stage, high-REE dolomite carbonatite (par – parisite-(Ce), dol – dolomite, py – pyrite; CDD2-26, 225.2 m). **b** Intergrown crystals of parisite-(Ce) and aeschynite-(Ce) (aesc) in dolomite carbonatite (note parisite-(Ce) overgrowths on primary crystal of parisite-(Ce); CDD2-26). **c** Grey, late stage, high-REE dolomite carbonatite dyke intruding white high-Sr calcite carbonatite (CDD2-25, 397.35 m). Contains patches of pink calcite-monazite-(Ce) (cc-mz) replacing apatite (ap, phl – phlogopite, amp – amphibole). **d** Calcite and monazite-(Ce) (mz) replacing apatite in high-REE dolomite carbonatite (CDD2-25; SEM-BSE image). **e** White low-Sr dolomite carbonatite containing vugs (CDD2-8, 152 m). **f** Crystals of synchysite-(Ce) (syn) and dolomite lining vug in low-Sr dolomite carbonatite (CDD2-18, 328.78 m).

**Fig. 6** Boundary between high REE apatite-monazite-(Ce) rock (ap-mz) and an adjacent comb-textured apatite vein with a dolomite (dol) carbonatite vein at the bottom of the image (thin section in transmitted light; CDD1, 270.33 m).

**Fig. 7 a** Texture of complex intergrowths in apatite-monazite-(Ce) rock (CDD1-33, 270.33 m; ap – apatite, mz – monazite-(Ce)). **b** Crystals of monazite-(Ce) in talc-amphibole (amp) matrix (CDD1-29, 265.3 m). **c** BSE image showing texture of complex monazite-(Ce)-apatite intergrowths (CDD1-33; pyrr – pyrrhotite). **d** BSE image showing texture of foliated monazite-(Ce)-amphibole-talc rock (CDD1-29). **e** Element map of complex monazite-(Ce)-apatite intergrowths illustrated in **c**. Red – apatite (P); purple – monazite-

(Ce) (Ce); green – talc, amphibole (Si); light blue – pyrrhotite (S); black – dolomite. **f** BSE image illustrating further complex intergrowths of monazite-(Ce) and apatite (CDD1-33).

**Fig. 8 a** SrO versus TREO, and **b** Chondrite-normalised REE patterns, for apatite from the high-REE apatite-monazite-(Ce) rock and carbonatites from the CRCC.

**Fig. 9 a** Chondrite-normalised REE patterns for the Cummins Range carbonatites. Average magnesiocarbonatite from Chakhmouradian et al. (2009). **b** Primitive mantle-normalised trace element diagram for the Cummins Range carbonatites (normalising data from Palme and O'Neill (2005)).

**Fig. 10** Stable carbon and oxygen isotope compositions (in ‰ relative to V-PDB and V-SMOW, respectively) for the Cummins Range carbonatite complex. Data for the Mt Weld carbonatite are from Nelson et al. (1988) and Graham et al. (2004). Boxes indicate the 'primary carbonatite fields' of Taylor et al. (1967; black) and Keller and Hoefs (1995; grey).

**Fig. 11** $H_2O$-contents (in ppm) and stable hydrogen isotope compositions of fluid inclusion-hosted $H_2O$ (in ‰ relative to V-SMOW), as well as bulk carbonate C and O isotope compositions (in ‰ relative to V-PDB and V-SMOW, respectively) for ten carbonate samples from the Cummins Range carbonatites. **a** $\delta$ D versus $H_2O$ contents trapped in fluid

1093 inclusions in host carbonates. **b** and **c**: $\delta$ D values of inclusion-hosted water versus $\delta^{13}C$

1094 (**b**) and $\delta^{18}O$ (**c**) values of the host carbonates.

1095

1096 **Fig. 12** Schematic diagram illustrating the evolution of the CRCC.

Figure 1
Click here to download high resolution image

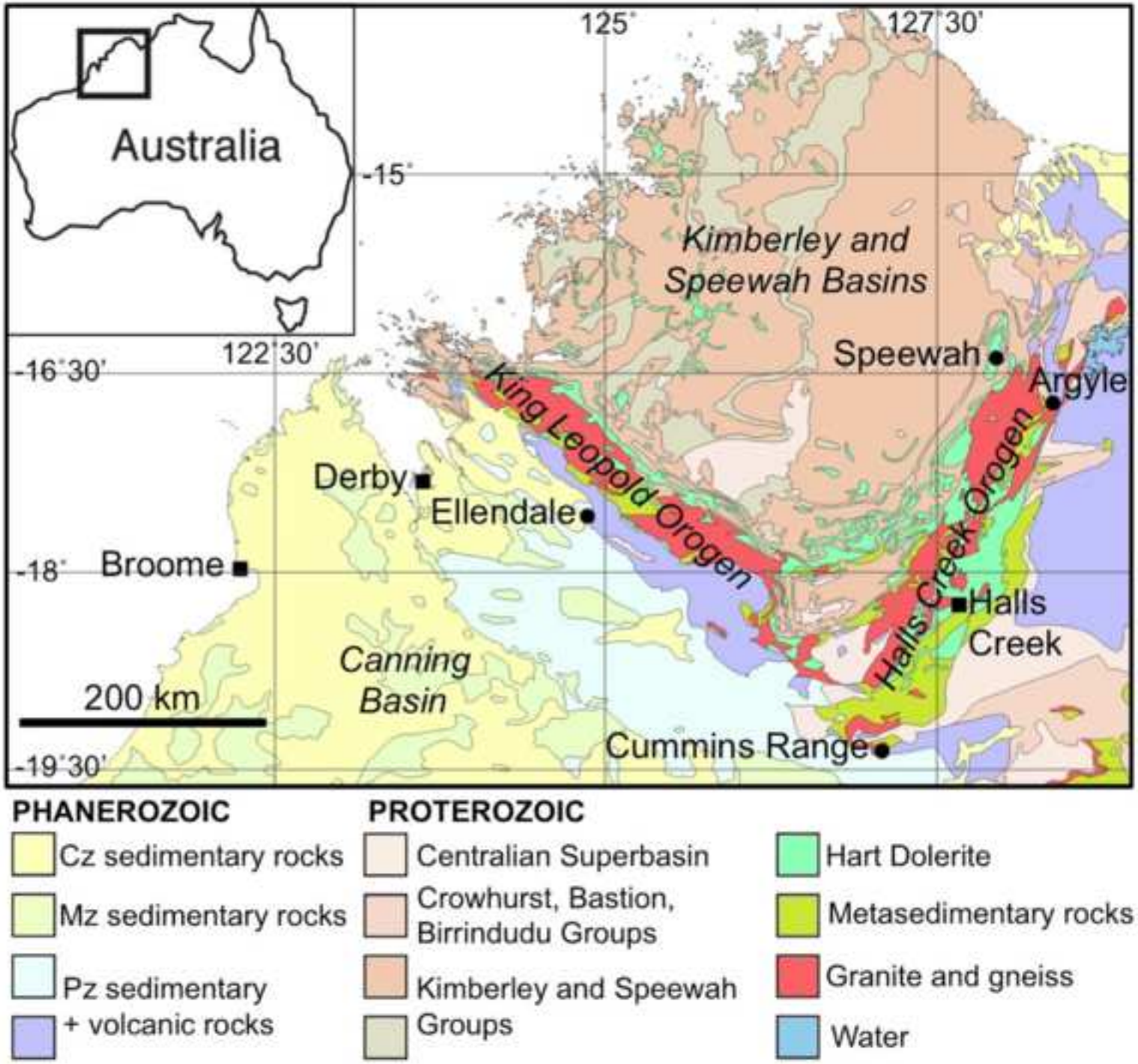

Figure 2

Click here to download high resolution image

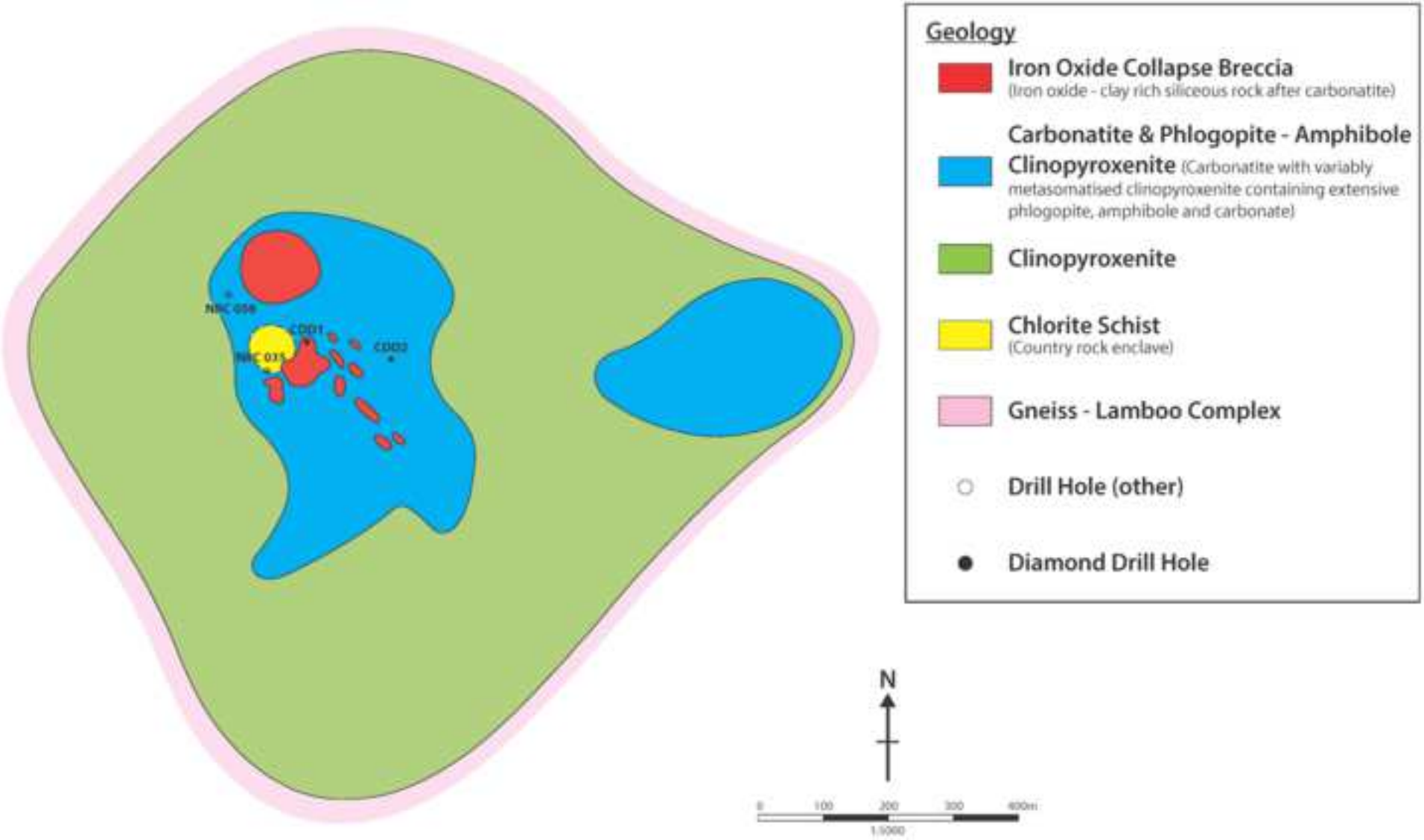

Figure 3

Click here to download high resolution image

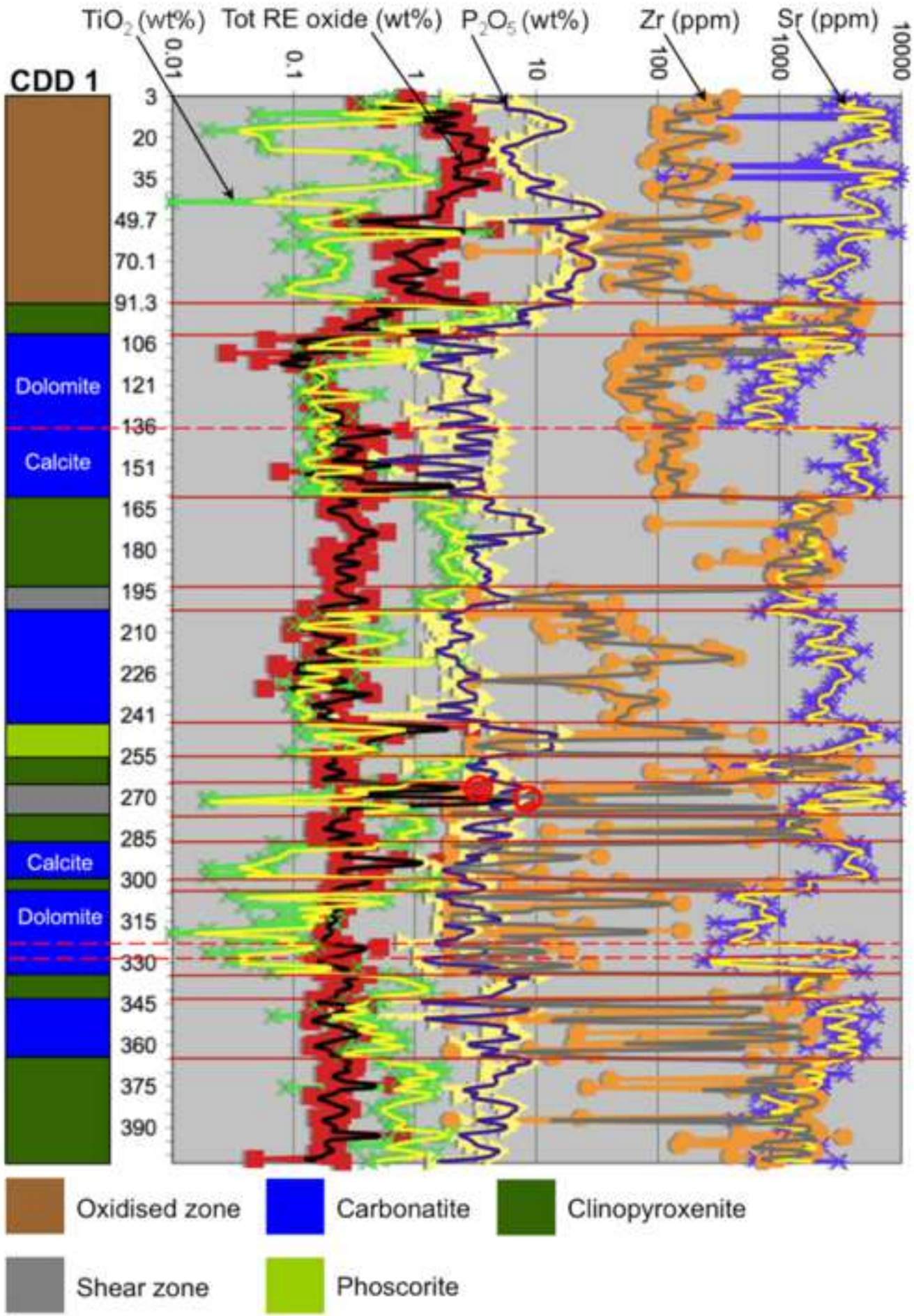

Figure 4
Click here to download high resolution image

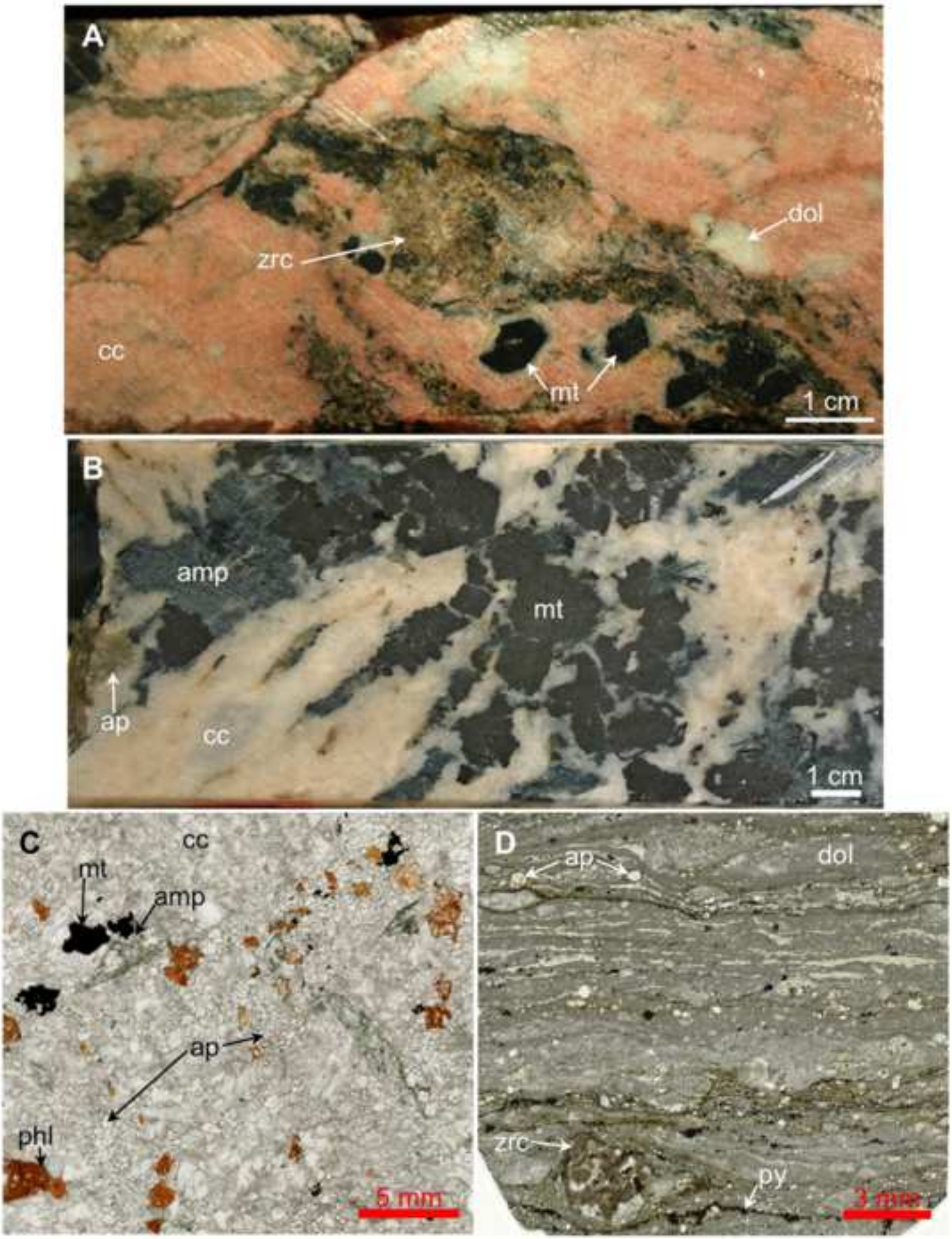

Figure 5
Click here to download high resolution image

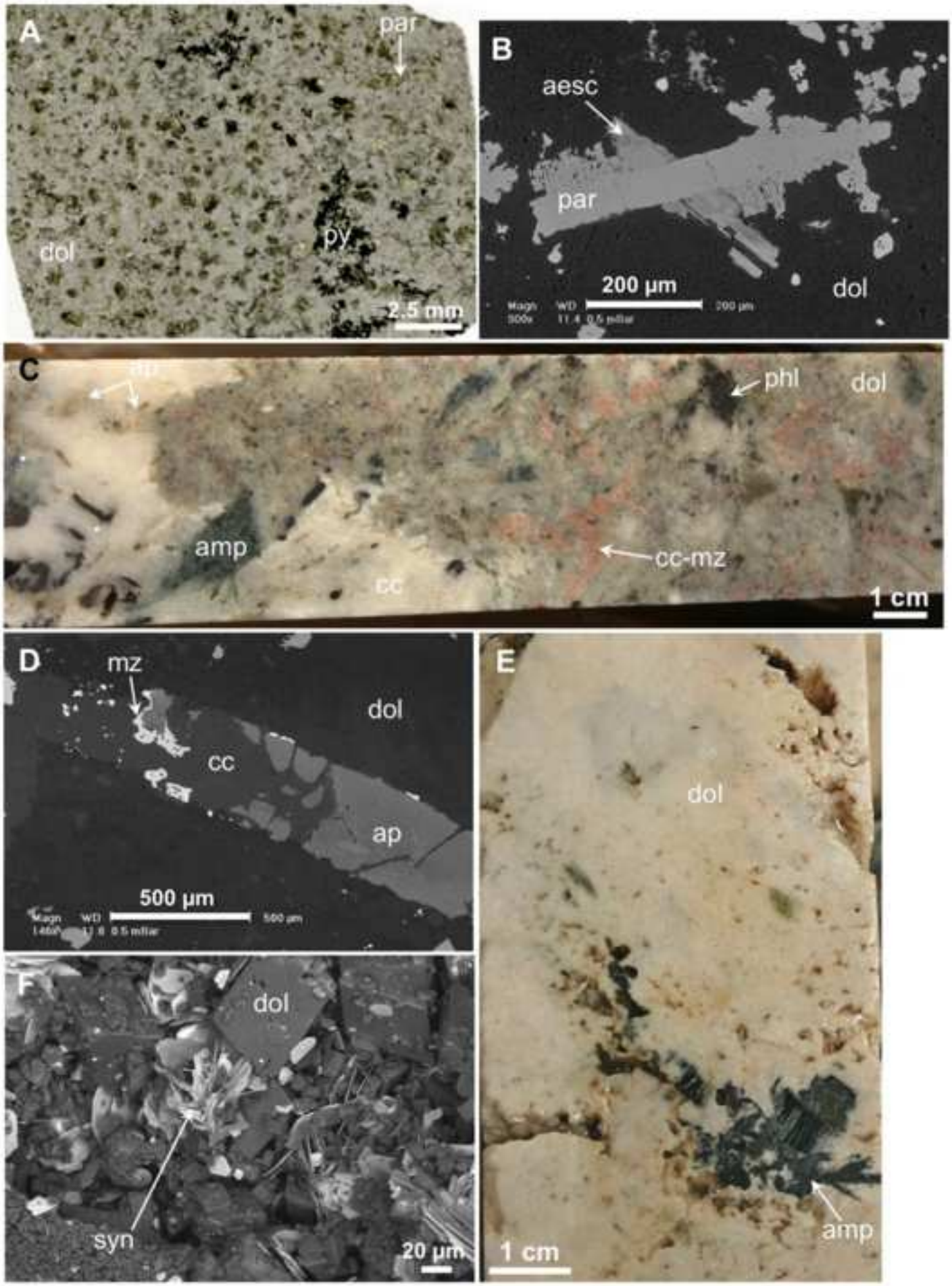

Figure 6
Click here to download high resolution image

Figure 7
Click here to download high resolution image

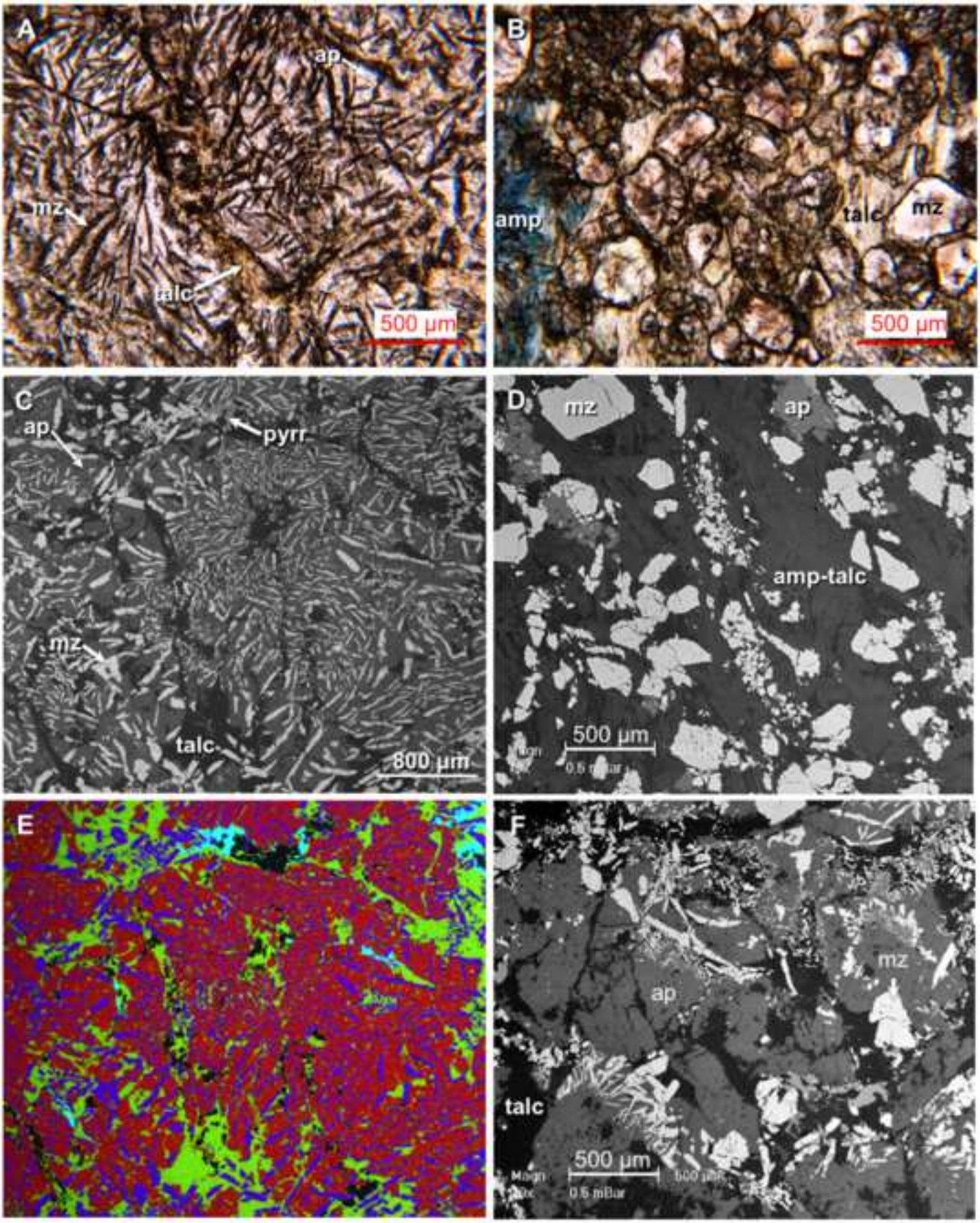

Figure 8

Click here to download high resolution image

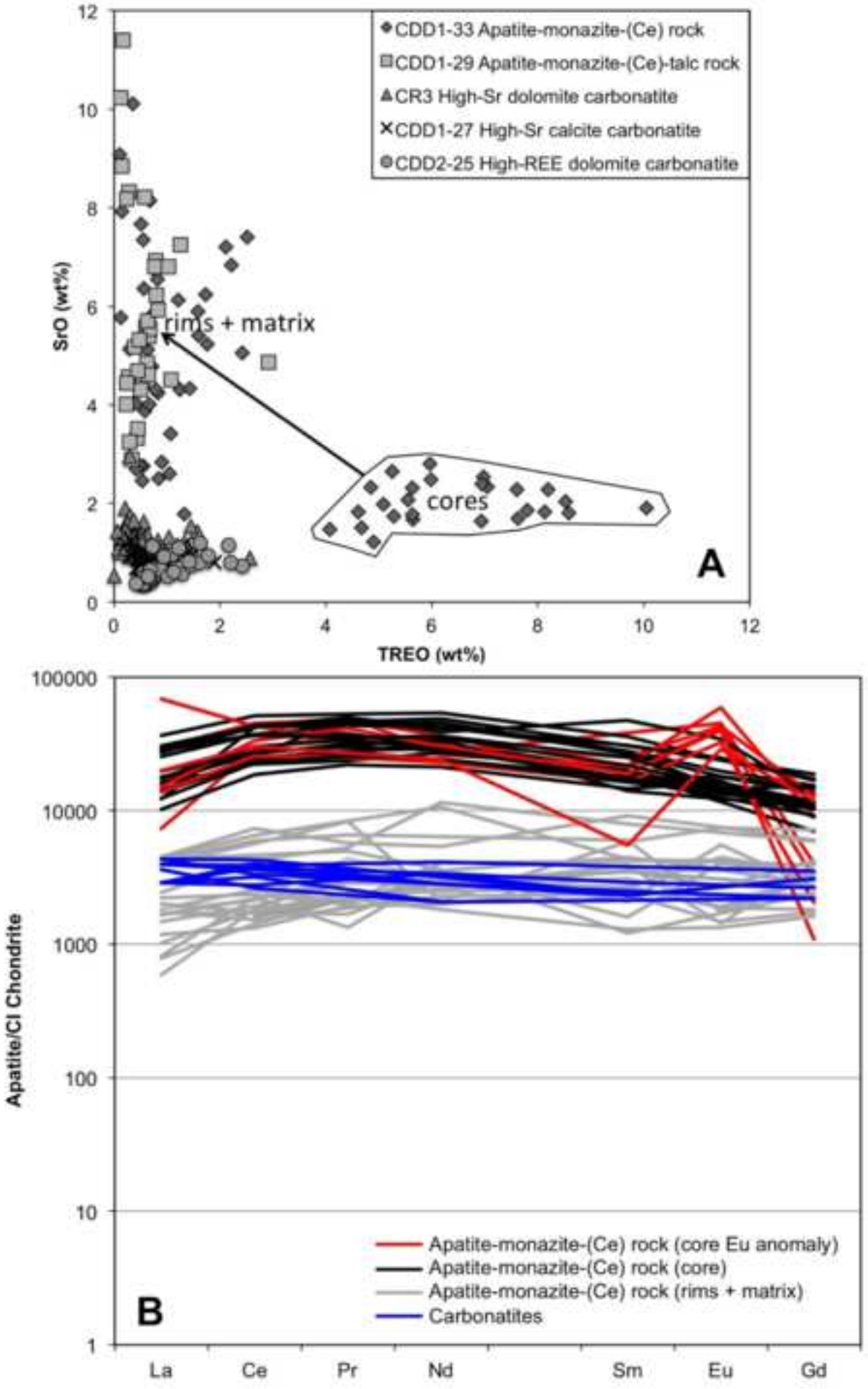

Figure 9

Click here to download high resolution image

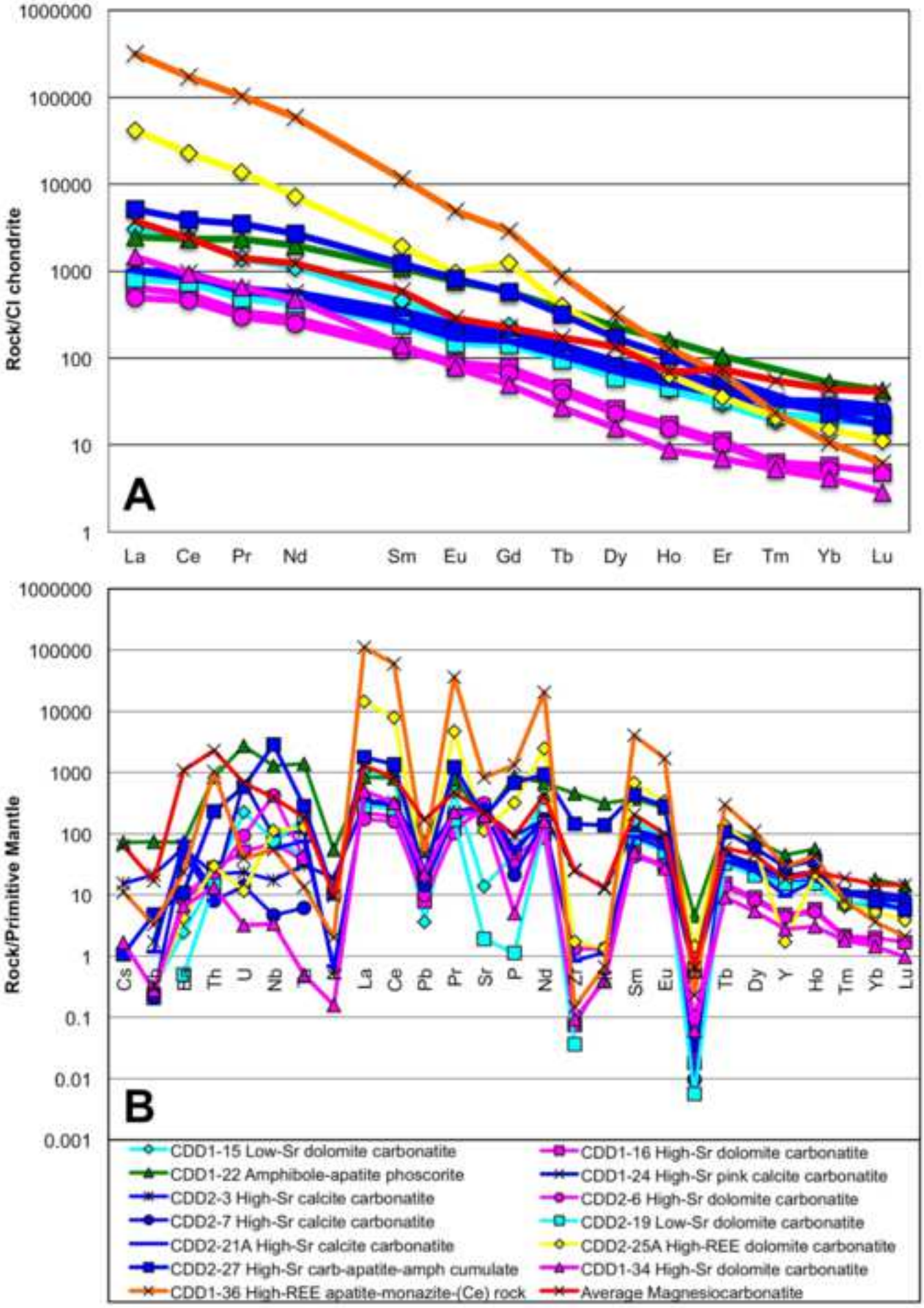

Figure 10
Click here to download high resolution image

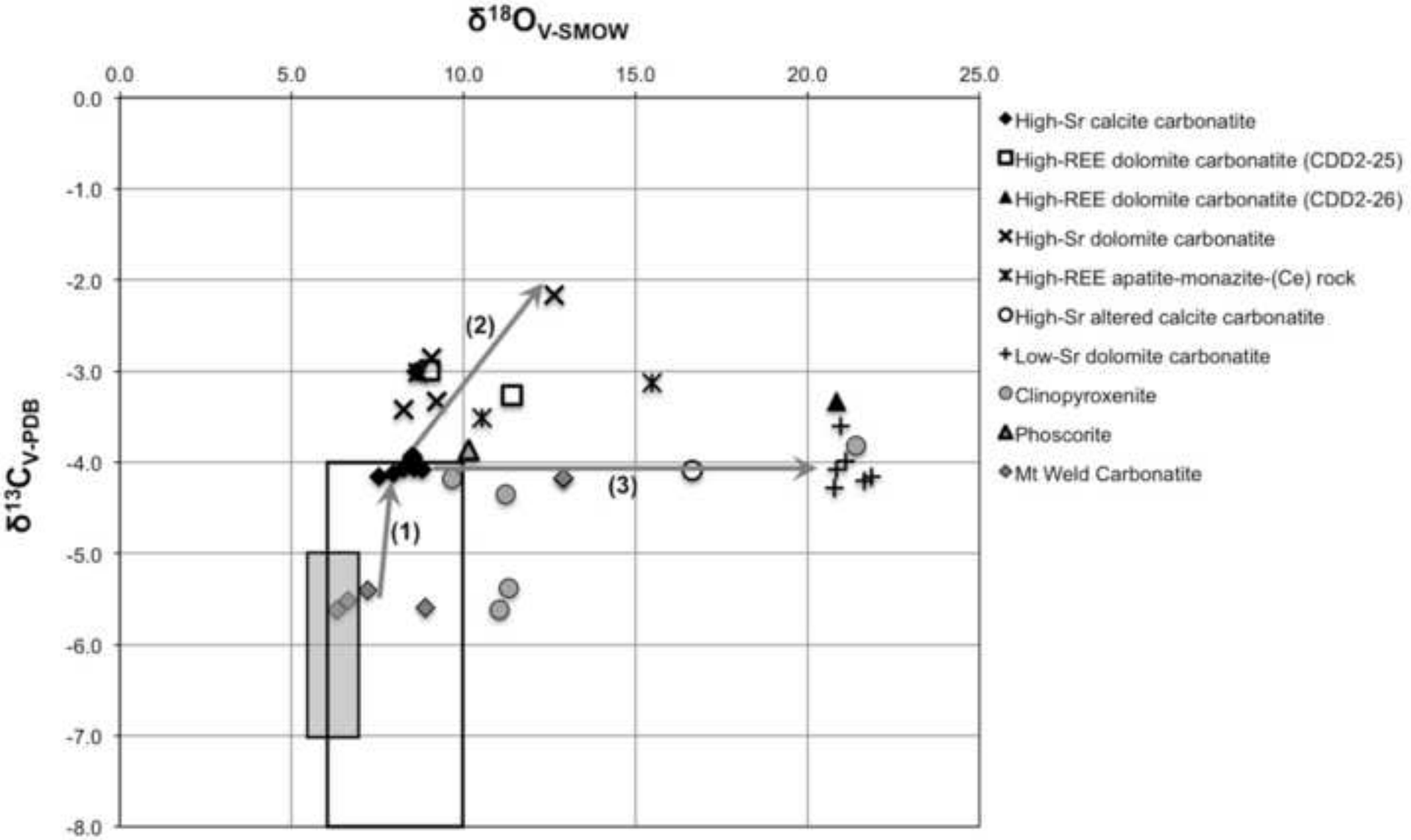

Figure 11
Click here to download high resolution image

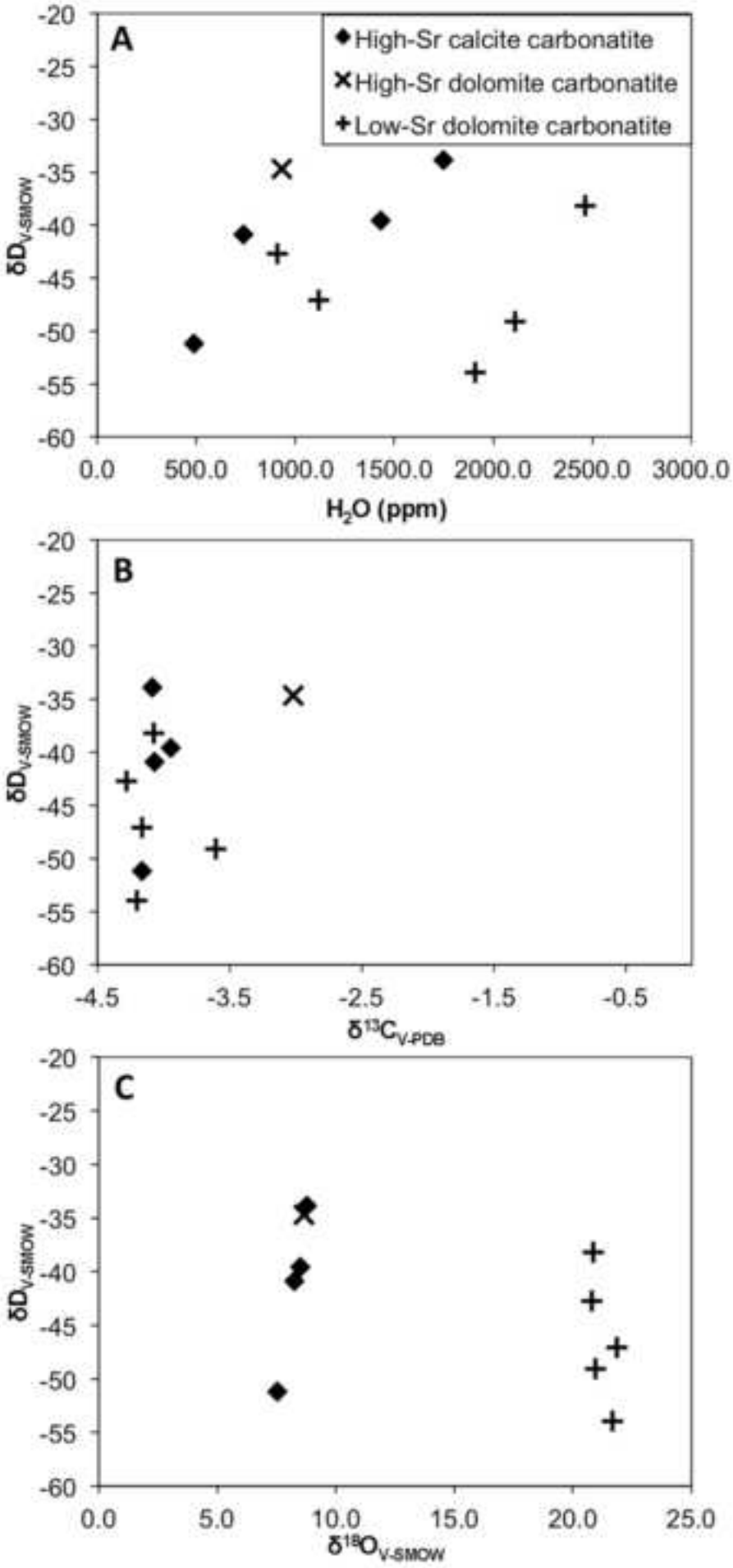

Figure 12
Click here to download high resolution image

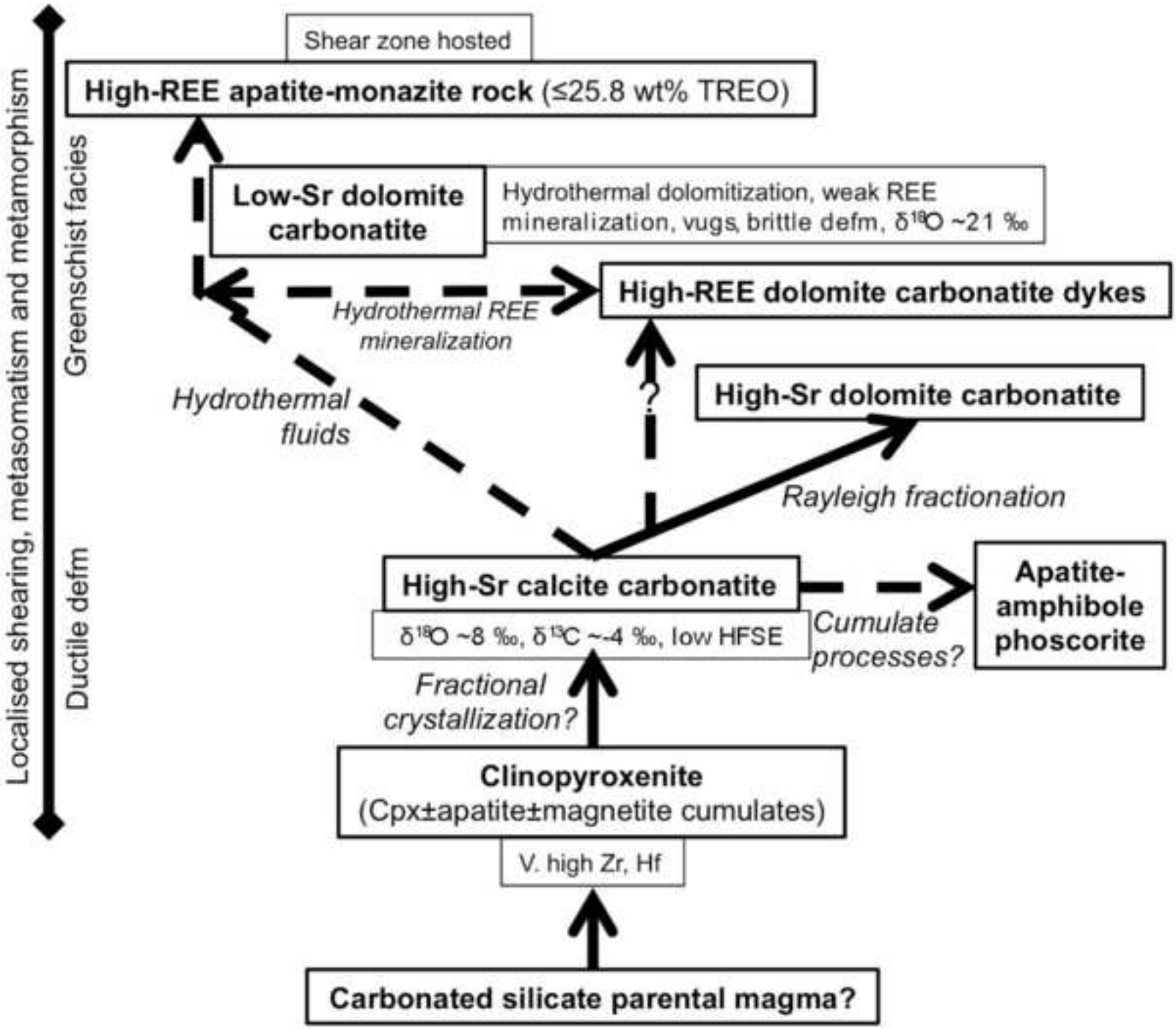

**Table 1** Mineralogy of the carbonatites and associated rocks from the Cummins Range Carbonatite Complex.

| Rock type | Texture | Mineralogy |
|---|---|---|
| **Clinopyroxenite** | Mesocumulate. Medium–coarse-grained. | Phlogopite, diopside, apatite, magnetite, ilmenite, richterite, calcite, dolomite, actinolite (replacing diopside). Pyrrhotite, pyrite, chalcopyrite, galena, sphalerite. Titanite, zirconolite, calzirtite, perovskite (partially–completely replaced by ilmenite, lucasite?, kassite, titanite), baddeleyite, nioboaeschynite-(Ce), monazite-(Ce), allanite-(Ce), zircon, barite. |
| **Phoscorite–series apatite-rich rocks** | Cumulate. Medium–coarse-grained, massive to banded and foliated metasomatised rocks. | Apatite, phlogopite, magnetite, richterite–magnesioriebeckite, dolomite, calcite, ilmenite. Pyrite, chalcopyrite, pyrrhotite, sphalerite. Zircon, pyrochlore, nioboaeschynite-(Ce), barite, fluorite. |
| **High-Sr calcite carbonatite** | White–light grey to pink. Massive to foliated. Bands of cumulate-textured apatite-phlog-amph-magnetite. | Calcite (≤5 mm), apatite (≤30%; ≤1.5 cm), magnetite (≤30%; ≤3 cm), ilmenite, phlogopite (≤1 cm), amphibole (≤5%; ≤1.3 cm; metasomatic), dolomite (≤5 mm). Pyrrhotite, pyrite, chalcopyrite, sphalerite, galena. Zircon, pyrochlore (≤5%, generally ≤1%; ≤10 mm), nioboaeschynite-(Ce), parisite-(Ce), synchysite-(Ce), barite, chevkinite-(Ce), fergusonite, zirconolite, thorianite? |
| **High-Sr dolomite carbonatite** | Massive, white, weakly–moderately fractured dolomite carbonatite. | Dolomite, calcite, strontianite, apatite (≤5%; ≤1.5 mm; crystal clusters ≤1 cm), pyrite (≤1%), pyrrhotite, chalcopyrite, pyrochlore, ilmenite, monazite-(Ce) (≤1%), parisite-(Ce), synchysite-(Ce), Ca-REE-Ba-Sr carbonates (burbankite or carbocernaite?) |
| **High-REE dolomite carbonatite (1)** | Massive, medium-grained grey dolomite carbonatite. | Dolomite, parisite-(Ce) (~15–20%; ≤3 mm), pyrite (≤0.6 mm), monazite-(Ce), aeschynite-(Ce) (≤0.8 mm), galena. |
| **High-REE dolomite carbonatite (2)** | Massive grey dolomite carbonatite. Pink calcite-monazite-(Ce) replacement textures after apatite. | Dolomite, calcite, apatite, phlogopite, magnetite, monazite-(Ce), parisite-(Ce), synchysite-(Ce), apatite, fergusonite, strontianite, Ca-REE-Ba-Sr carbonates (burbankite or carbocernaite?) |
| **Low-Sr dolomite carbonatite** | White–grey foliated to massive with vugs. | Dolomite (≤2 cm), calcite, apatite, magnetite, phlogopite, amphibole, quartz. Pyrite, marcasite, chalcopyrite, sphalerite. Monazite-(Ce), parisite-(Ce), synchysite-(Ce), nioboaeschynite-(Ce), zircon, baddeleyite, pyrochlore, ferrocolumbite. |
| **High-REE apatite-monazite-(Ce) rock** | Complex intergrown apatite-monazite-(Ce) texture. Massive to foliated. Interval includes foliated monazite-(Ce)-talc rocks. | Apatite, monazite-(Ce), talc, amphibole, dolomite. Pyrrhotite, pyrite, chalcopyrite (≤5% sulfide mineralization along fractures). |

**Table 2** Representative analyses of apatite from the CRCC.

| | **Apatite-monazite-(Ce) rock** | | | | | **Carbonatites** | | |
|---|---|---|---|---|---|---|---|---|
| Sample No. | CDD1-33 | CDD1-33 | CDD1-33 | CDD1-33 | CDD1-29 | CR3 | CDD2-25 | CDD1-27 |
| Analysis No. | Area 3-1 A13 | Area 3-3 A2 | Area 3-2 A8 | Area 3-2 A9 | Area 4 A10 | Area 1 A2 | A1-4 | A6 |
| (wt%) | core | core | core | rim | matrix | | core | |
| $Na_2O$ | n.a. | n.a. | n.a. | n.a. | n.a. | 0.22 | 0.17 | 0.23 |
| MgO | n.a. | n.a. | n.a. | n.a. | n.a. | 0.17 | - | - |
| $Al_2O_3$ | - | - | 0.08 | 0.01 | - | - | - | - |
| $SiO_2$ | - | 0.01 | - | - | - | 0.05 | 0.28 | - |
| $P_2O_5$ | 38.96 | 39.00 | 38.94 | 40.18 | 38.21 | 41.00 | 42.22 | 43.31 |
| CaO | 48.54 | 50.08 | 46.32 | 50.80 | 47.00 | 55.18 | 54.32 | 52.19 |
| MnO | - | - | - | 0.02 | 0.02 | - | - | - |
| FeO | 0.03 | 0.05 | 0.02 | 0.03 | 0.15 | - | - | - |
| SrO | 2.07 | 1.22 | 2.04 | 5.83 | 11.39 | 0.94 | 0.43 | 1.15 |
| $Y_2O_3$ | 0.30 | 0.31 | 0.27 | 0.02 | - | 0.02 | 0.02 | - |
| $La_2O_3$ | 0.20 | 0.38 | 1.90 | 0.05 | 0.01 | 0.14 | 0.13 | 0.23 |
| $Ce_2O_3$ | 2.07 | 1.85 | 3.10 | 0.16 | 0.05 | 0.38 | 0.28 | 0.63 |
| $Pr_2O_3$ | 0.41 | 0.27 | 0.37 | 0.03 | - | 0.05 | 0.05 | 0.11 |
| $Nd_2O_3$ | 1.39 | 1.23 | 1.65 | 0.19 | - | 0.22 | 0.14 | 0.27 |
| $Sm_2O_3$ | 0.38 | 0.28 | 0.43 | 0.03 | - | - | - | - |
| $Eu_2O_3$ | 0.38 | 0.21 | 0.28 | 0.03 | 0.01 | - | - | - |
| $Gd_2O_3$ | 0.20 | 0.05 | 0.29 | 0.08 | - | 0.05 | 0.04 | 0.06 |
| $ThO_2$ | - | 0.02 | - | 0.01 | - | - | - | - |
| $UO_2$ | 0.01 | 0.01 | - | - | - | - | - | - |
| $SO_3$ | - | - | - | 0.03 | 0.03 | - | 0.04 | - |
| Cl | - | - | - | 0.01 | - | - | - | - |
| F | 3.74 | 3.38 | 3.61 | 3.92 | 3.49 | 3.65 | 4.21 | 4.42 |
| F,Cl=O | -1.57 | -1.43 | -1.52 | -1.65 | -1.47 | -1.54 | -1.77 | -1.86 |
| Total | 97.10 | 96.94 | 97.79 | 99.77 | 98.90 | 100.53 | 100.56 | 100.74 |
| **Structural formulae calculated to 26 (O,OH,F,Cl)** | | | | | | | | |
| Na | n.a. | n.a. | n.a. | n.a. | n.a. | 0.072 | 0.056 | 0.075 |
| Mg | n.a. | n.a. | n.a. | n.a. | n.a. | 0.043 | - | - |
| Al | - | - | 0.016 | 0.001 | - | - | - | - |
| Si | - | 0.002 | - | - | - | 0.008 | 0.047 | - |
| P | 5.650 | 5.657 | 5.648 | 5.828 | 5.542 | 5.847 | 6.021 | 6.177 |
| Ca | 8.909 | 9.192 | 8.501 | 9.325 | 8.627 | 9.959 | 9.804 | 9.420 |
| Mn | - | - | - | 0.002 | 0.003 | - | - | - |
| Fe | 0.005 | 0.006 | 0.003 | 0.004 | 0.022 | - | - | - |
| Sr | 0.206 | 0.121 | 0.202 | 0.579 | 1.132 | 0.092 | 0.042 | 0.112 |
| Y | 0.027 | 0.029 | 0.024 | 0.002 | - | 0.002 | 0.002 | 0.000 |
| La | 0.013 | 0.024 | 0.120 | 0.003 | 0.001 | 0.009 | 0.008 | 0.014 |
| Ce | 0.130 | 0.116 | 0.195 | 0.010 | 0.003 | 0.023 | 0.017 | 0.039 |
| Pr | 0.026 | 0.017 | 0.023 | 0.002 | - | 0.003 | 0.003 | 0.007 |
| Nd | 0.085 | 0.075 | 0.101 | 0.012 | - | 0.013 | 0.008 | 0.016 |
| Sm | 0.022 | 0.017 | 0.026 | 0.002 | - | - | - | - |
| Eu | 0.022 | 0.012 | 0.016 | 0.002 | 0.000 | - | - | - |
| Gd | 0.012 | 0.003 | 0.017 | 0.004 | - | 0.003 | 0.002 | 0.003 |
| Th | - | 0.001 | - | 0.000 | - | - | - | - |
| U | 0.000 | 0.000 | - | - | - | - | - | - |
| S | - | - | - | 0.004 | 0.004 | - | 0.005 | - |
| Cl | 0.000 | 0.001 | - | 0.003 | - | - | - | - |
| F | 2.025 | 1.833 | 1.957 | 2.125 | 1.892 | 1.944 | 2.243 | 2.355 |
| A-site | 9.456 | 9.613 | 9.229 | 9.946 | 9.788 | 10.219 | 9.943 | 9.687 |
| B-site | 5.650 | 5.659 | 5.664 | 5.833 | 5.546 | 5.856 | 6.069 | 6.177 |

(- = below detection limits; n.a. = not analysed)

**Table 3** Representative whole-rock geochemistry of carbonatites and associated apatite-rich rocks from the CRCC.

| Sample No. | CDD1-16 | CDD1-22 | CDD2-19 | CDD2-21A | CDD2-25A | CDD2-27 | CDD1-34 | CDD1-36 |
|---|---|---|---|---|---|---|---|---|
| Depth | 150.82 – 151.03 m | 251.13 – 251.22 m | 370 – 370.15 m | 399.78 – 399.95 m | 397.45 – 397.59 m | 400.5 – 400.68 m | 263.75 – 263.85 m | 269.75 m |
| | High-Sr dolomite carbonatite | Amphibole-apatite phoscorite | Low-Sr dolomite carbonatite | High-Sr calcite carbonatite | High-REE dolomite-calcite carbonatite | High-Sr carbonatite-apatite-amph cumulate | High-Sr dolomite carbonatite | High-REE apatite-monazite-(Ce) rock |
| (wt%) | | | | | | | | |
| $SiO_2$ | 0.023 | 17.79 | <0.01 | 0.29 | 0.292 | 8.27 | 3.49 | 8.55 |
| $TiO_2$ | 0.012 | 0.975 | 0.008 | 0.136 | 0.305 | 0.131 | 0.013 | 0.049 |
| $Al_2O_3$ | <0.01 | 2.00 | <0.01 | 0.031 | <0.01 | 0.108 | 0.095 | 0.207 |
| $Fe_2O_3$ | 0.67 | 1.56 | 0.36 | 0.56 | 2.32 | 1.84 | 1.70 | 0.890 |
| FeO | 3.84 | 2.98 | 1.95 | 0.76 | 4.60 | 2.62 | 18.9 | 1.10 |
| MnO | 0.793 | 0.168 | 0.272 | 0.183 | 0.822 | 0.501 | 0.683 | 0.116 |
| MgO | 19.0 | 9.03 | 21.3 | 1.41 | 12.0 | 11.7 | 12.7 | 4.01 |
| CaO | 30.9 | 31.5 | 31.1 | 55.4 | 33.9 | 33.8 | 21.2 | 20.9 |
| $Na_2O$ | 0.082 | 1.04 | 0.061 | 0.034 | 0.126 | 1.05 | 0.167 | 0.352 |
| $K_2O$ | 0.006 | 1.72 | 0.004 | 0.029 | 0.009 | 0.329 | 0.005 | 0.062 |
| $P_2O_5$ | 0.92 | 17.05 | 0.035 | 1.25 | 7.28 | 13.4 | 0.099 | 26.1 |
| SrO | 0.601 | 0.415 | 0.005 | 0.689 | 0.270 | 0.454 | 0.484 | 2.00 |
| TREO | 0.085 | 0.440 | 0.125 | 0.138 | 3.43 | 0.671 | 0.142 | 25.8 |
| $SO_3$ | 0.443 | 0.187 | 0.277 | 0.038 | 0.012 | 0.036 | 19.8 | 0.352 |
| LOI | 44.0 | 10.3 | 46.3 | 41.4 | 34.8 | 24.4 | 18.9 | 3.71 |
| F | 0.111 | 2.02 | 0.040 | 0.512 | 0.720 | 1.39 | <0.01 | 1.22 |
| Cl (ppm) | 197 | 37 | 448 | 173 | 239 | 65 | 246 | 59 |
| Total | 101.5 | 99.2 | 101.8 | 102.9 | 100.9 | 100.7 | 98.1 | 95.5 |

**Table 4** Trace-element geochemistry of carbonatites and associated apatite-rich rocks from the CRCC (samples CDD1-22, CDD2-27, CDD1-34, CDD1-36 analysed at Geoscience Australia and ANU).

| Sample No. | CDD1-15 | CDD1-16 | CDD1-22 | CDD1-24 | CDD2-3 | CDD2-6 | CDD2-7 | CDD2-19 | CDD2-21A | CDD2-25A | CDD2-27 | CDD1-34 | CDD1-36 |
|---|---|---|---|---|---|---|---|---|---|---|---|---|---|
| Depth | 133.7 – 133.95 m Low-Sr dol carb | 150.82 – 151.03 m High-Sr dol carb | 251.13 – 251.22 m Amph-apatite phoscorite | 288.95 – 289.2 m High-Sr calcite carb | 82.25 – 82.4 m High-Sr calcite carb | 113.9 – 114 m High-Sr dol carb | 128.15 – 128.3 m High-Sr calcite carb | 370 – 370.15 m Low-Sr dol carb | 399.78 – 399.95 m High-Sr calcite carb | 397.45 – 397.59 m High-REE dol-calcite carb | 400.5 – 400.68 m High-Sr carb-apatite-amph cumulate | 263.75 – 263.85 m High-Sr dol carb | 269.75 m High-REE apatite-monazite-(Ce) rock |
| (ppm) | | | | | | | | | | | | | |
| Li | 1.35 | 1.35 | n.a. | 5.74 | 6.88 | 0.885 | 0.61 | 0.274 | 1.47 | 1.73 | n.a. | n.a. | n.a. |
| Be | 0.284 | < 0.100 | 5.95 | 0.242 | 0.307 | < 0.100 | 0.479 | < 0.100 | < 0.100 | 0.254 | 2.95 | 0.3 | 1.70 |
| B | < 0.100 | 5.91 | n.a. | 5.34 | 1.24 | 1.79 | 13.2 | 6.84 | 17.7 | 11.9 | n.a. | n.a. | n.a. |
| V | 3.59 | 1.29 | 77.2 | 0.949 | 29.8 | 1.87 | 0.773 | < 0.100 | 14.9 | 37.1 | 34.3 | 4.0 | 4.0 |
| Cr | 2.33 | 0.563 | 24.9 | 4.01 | 0.475 | 0.549 | 0.617 | 3.59 | 0.8 | 5.47 | 13.8 | 22 | 77 |
| Co | 8.32 | 4.41 | 12 | 5.73 | 7.7 | 4.8 | 4.45 | 4.36 | 3.86 | 7.14 | 8.18 | 150 | 22 |
| Ni | 1.1 | 1.31 | 16 | 7.31 | 2.25 | < 0.100 | 4.93 | 2.05 | 4.73 | < 0.100 | 12.2 | 20 | 24 |
| Cu | 37 | 7.76 | 127 | 56.4 | 10.6 | 1.8 | 2.52 | < 0.100 | 14.4 | 9.58 | 73.9 | 1890 | 28 |
| Zn | 5.01 | 20.1 | 101 | 9.92 | 9.29 | 28.5 | 2.94 | 0.6 | 7.1 | 36.1 | 33.7 | 44 | 79 |
| Ga | 33.1 | 5.42 | 22.2 | 10.7 | 14.4 | 5.14 | 9.41 | 8.07 | 6.38 | 32.6 | 20.1 | 4.0 | 25.0 |
| Ge | 3.84 | 0.961 | 1.6 | 1.99 | 1.9 | 0.933 | 1.83 | 1.55 | 1.24 | 2.89 | 1.56 | 0.2 | 1.7 |
| As | 7.88 | 4.79 | 3.5 | 4.14 | 1.84 | 1.33 | 7.05 | 2.33 | 17.3 | 8.12 | 2.85 | 1.5 | 11.0 |
| Se | 4.94 | 2.31 | n.a. | 6.76 | 5.52 | 2.64 | 6.55 | 4.84 | 3.92 | 2.42 | n.a. | n.a. | n.a. |
| Rb | 0.182 | 0.127 | 44.6 | 1.03 | 12.7 | 0.133 | 0.132 | < 0.100 | 0.708 | 0.168 | 2.88 | 0.17 | 2.0 |
| Sr | 282 | 5080 | 3507 | 6060 | 4800 | 6310 | 5060 | 38.5 | 5830 | 2280 | 3843 | 4090 | 16897 |
| Y | 51.4 | 20.7 | 194 | 90.3 | 70.2 | 19.1 | 84.8 | 67 | 42 | 7.46 | 124 | 12 | 126 |
| Zr | < 0.100 | 0.816 | 4879 | 279 | 0.871 | 14 | < 0.100 | 0.395 | 8.92 | 18.5 | 1544 | 1 | 1.6 |
| Nb | 47.9 | 42 | 764 | 55.2 | 10.4 | 254 | 2.82 | 41.7 | 34.1 | 67.3 | 1719 | 1.92 | 25 |
| Mo | 0.337 | 0.233 | 0.33 | < 0.100 | < 0.100 | < 0.100 | < 0.100 | 0.121 | 0.233 | 0.187 | 0.141 | 1.36 | 0.23 |
| Ag | n.a. | n.a. | 1.59 | n.a. | n.a. | n.a. | n.a. | n.a. | n.a. | n.a. | 0.328 | 1.3 | 0.2 |
| Cd | < 0.100 | 0.355 | 1.50 | 0.339 | 0.186 | 0.793 | 0.25 | < 0.100 | 0.202 | 0.379 | 0.862 | 0.40 | 0.20 |
| In | < 0.100 | 0.128 | n.a. | 0.131 | < 0.100 | 0.241 | < 0.100 | < 0.100 | < 0.100 | 0.25 | n.a. | n.a. | n.a. |
| Sn | 0.165 | 0.154 | 3.2 | < 0.100 | 0.289 | 0.208 | < 0.100 | 0.614 | 0.203 | 0.562 | 3.01 | 1.5 | 0.6 |
| Sb | < 0.100 | < 0.100 | 0.08 | < 0.100 | < 0.100 | < 0.100 | < 0.100 | 0.355 | < 0.100 | < 0.100 | 0.106 | 1 | 4 |

**Table 4** Trace-element geochemistry of carbonatites and associated apatite-rich rocks from the CRCC (samples CDD1-22, CDD2-27, CDD1-34, CDD1-36 analysed at Geoscience Australia and ANU).

| Sample No. (ppm) | CDD1-15 | CDD1-16 | CDD1-22 | CDD1-24 | CDD2-3 | CDD2-6 | CDD2-7 | CDD2-19 | CDD2-21A | CDD2-25A | CDD2-27 | CDD1-34 | CDD1-36 |
|---|---|---|---|---|---|---|---|---|---|---|---|---|---|
| Cs | < 0.100 | < 0.100 | 1.29 | < 0.100 | 0.279 | < 0.100 | < 0.100 | < 0.100 | < 0.100 | < 0.100 | 0.019 | 0.03 | 0.2 |
| Ba | 16.3 | 62 | 490 | 419 | 397 | 57 | 325 | 3.32 | 509 | 28.4 | 73.3 | 44 | 158 |
| La | 717 | 152 | 580 | 239 | 201 | 117 | 210 | 195 | 240 | 9860 | 1216 | 345 | 75020 |
| Ce | 1490 | 338 | 1440 | 586 | 500 | 284 | 510 | 457 | 515 | 14200 | 2408 | 567 | 106220 |
| Pr | 131 | 31.8 | 216 | 58.7 | 51.6 | 27.6 | 51.7 | 44.7 | 61.5 | 1280 | 327 | 61 | 9650 |
| Nd | 508 | 130 | 895 | 260 | 227 | 113 | 230 | 193 | 209 | 3280 | 1233 | 213 | 26904 |
| Sm | 68.5 | 20.3 | 161 | 51.3 | 43.5 | 18.4 | 45.4 | 35.5 | 38.8 | 288 | 184 | 21 | 1735 |
| Eu | 13.6 | 4.98 | 42.9 | 13.6 | 11.4 | 4.71 | 11.9 | 8.3 | 9.41 | 53.9 | 45.7 | 4.4 | 276 |
| Gd | 46.8 | 15.5 | 115 | 40.4 | 32.5 | 13.1 | 34.9 | 28.2 | 31.3 | 244 | 113 | 9.85 | 571 |
| Tb | 4.29 | 1.62 | 13.25 | 5.03 | 3.95 | 1.42 | 4.44 | 3.38 | 3.78 | 14.3 | 11.3 | 0.96 | 31 |
| Dy | 16.1 | 6.4 | 55.7 | 22.4 | 16.8 | 5.65 | 19.7 | 14.6 | 17.4 | 43.6 | 41.7 | 3.84 | 78 |
| Ho | 2.32 | 0.926 | 8.82 | 3.81 | 2.75 | 0.835 | 3.35 | 2.47 | 2.78 | 3.49 | 5.78 | 0.48 | 7.03 |
| Er | 4.75 | 1.79 | 16.8 | 8.17 | 5.8 | 1.62 | 7.28 | 5.35 | 6.07 | 5.71 | 9.68 | 1.11 | 10.5 |
| Tm | 0.466 | 0.155 | n.a. | 0.811 | 0.545 | 0.145 | 0.718 | 0.535 | 0.746 | 0.508 | n.a. | 0.13 | 0.58 |
| Yb | 3.05 | 0.922 | 8.33 | 5.09 | 3.32 | 0.817 | 4.47 | 3.42 | 3.9 | 2.41 | 3.65 | 0.66 | 1.68 |
| Lu | 0.42 | 0.119 | 1.03 | 0.682 | 0.429 | < 0.100 | 0.594 | 0.459 | 0.56 | 0.276 | 0.410 | 0.07 | 0.15 |
| Hf | < 0.100 | < 0.100 | 93 | 3.81 | 0.136 | 0.388 | < 0.100 | < 0.100 | 0.345 | 0.4 | 41.1 | 0.127 | 0.20 |
| Ta | 1.74 | 1.44 | 55 | 4.37 | 1.24 | 1.6 | 0.246 | 7.39 | 3.03 | 5.06 | 11.3 | 0.02 | 0.54 |
| W | 19.4 | 17.5 | 9 | 13.7 | 42.7 | 26 | 26.7 | 23.9 | 21.4 | 35.3 | 20.4 | 58 | 32 |
| Tl | < 0.100 | < 0.100 | n.a. | < 0.100 | < 0.100 | < 0.100 | < 0.100 | < 0.100 | < 0.100 | < 0.100 | n.a. | n.a. | n.a. |
| Pb | 0.664 | 1.44 | 13.1 | 7.92 | 2.99 | 1.87 | 2.66 | < 0.100 | 3.40 | 3.57 | 4.00 | 4.00 | 7.25 |
| Bi | < 0.100 | < 0.100 | 0.065 | < 0.100 | < 0.100 | < 0.100 | < 0.100 | < 0.100 | < 0.100 | < 0.100 | 0.073 | 0.02 | <0.02 |
| Th | 1.58 | 2.25 | 70 | 0.965 | 1.8 | 1.52 | 0.669 | 1.2 | 0.666 | 2.42 | 19.4 | 1.1 | 85 |
| U | 4.97 | 1.1 | 60 | 15 | 0.505 | 2.02 | 0.3 | < 0.100 | < 0.100 | 0.253 | 12.7 | 0.07 | 0.86 |
| Sc | 14 | 10.3 | 13.1 | 21.1 | 7.12 | 12.4 | 14.7 | 8.2 | 3.42 | 0.187 | 56.7 | 20.0 | 45.0 |
| Zr/Hf | - | - | 52.5 | 73.2 | 6.40 | 36.1 | - | - | 25.9 | 46.3 | 37.6 | 7.87 | 8.00 |
| Nb/Ta | 27.5 | 29.2 | 13.9 | 12.6 | 8.39 | 159 | 11.5 | 5.64 | 11.3 | 13.3 | 152 | 96.0 | 46.3 |
| Th/U | 0.318 | 2.05 | 1.17 | 0.064 | 3.56 | 0.752 | 2.23 | - | - | 9.57 | 1.53 | 15.7 | 98.8 |
| Ga/Ge | 8.62 | 5.64 | 13.6 | 5.38 | 7.58 | 5.51 | 5.14 | 5.21 | 5.15 | 11.3 | 12.9 | 17.4 | 14.7 |
| Y/Ho | 22.2 | 22.4 | 22.0 | 23.7 | 25.5 | 22.9 | 25.3 | 27.1 | 15.1 | 2.14 | 21.5 | 25.0 | 17.9 |

(n.a. – not analysed)

**Table 5** Stable C and O isotope compositions (in ‰ relative to V-PDB and V-SMOW, respectively) of carbonatites and associated rocks from the CRCC.

| Sample No. | Hole No. | Depth (m) | Rock type | $\delta^{13}C$ | $\delta^{18}O$ |
|---|---|---|---|---|---|
| CR3 | CDD1 | 151.8–151.94 | High-Sr dol carb | -3.4 | 8.3 |
| CR10 | CDD1 | 324–324.1 | High-Sr pink cc carb | -4.1 | 8.6 |
| CR14 | CDD1 | 401.65–401.75 | High-Sr cc carb | -4.1 | 8.0 |
| CDD2-3 | CDD2 | 82.25–82.4 | High-Sr cc carb | -4.1 | 8.3 |
| CDD2-6 | CDD2 | 113.9–114 | High-Sr dol carb | -3.0 | 8.7 |
| CDD2-7 | CDD2 | 128.15–128.3 | High-Sr cc carb | -4.1 | 8.8 |
| CDD2-9 | CDD2 | 178.05–178.15 | High-Sr cc carb | -4.0 | 8.5 |
| CDD2-22 | CDD2 | 401.9–402 | High-Sr cc carb | -4.2 | 7.5 |
| NRC-35 | NRC035 | 92–93 | Dol carb | -3.3 | 9.2 |
| NRC-58 | NRC058 | 97–98 | High-Sr cc carb | -3.0 | 8.6 |
| CR7 | CDD1 | 235.84–235.94 | Dol carb | -2.2 | 12.6 |
| CR12 | CDD1 | 375–375.1 | High-Sr cc carb | -4.1 | 16.7 |
| CR13 | CDD1 | 386–386.1 | Low-Sr dol carb | -4.0 | 21.1 |
| CDD2-1 | CDD2 | 69.5–69.65 | Low-Sr dol carb | -4.1 | 20.9 |
| CDD2-10 | CDD2 | 199–199.15 | Low-Sr dol carb | -4.2 | 21.7 |
| CDD2-12 | CDD2 | 225.65–225.8 | Low-Sr dol carb | -3.6 | 21.0 |
| CDD2-18 | CDD2 | 328.78–328.94 | Low-Sr dol carb | -4.2 | 21.9 |
| CDD2-19 | CDD2 | 370–370.15 | Low-Sr dol carb | -4.3 | 20.8 |
| CDD2-25 cc | CDD2 | 397.35–397.45 | High-REE dol carb | -3.3 | 11.4 |
| CDD2-25 dol | CDD2 | 397.35–397.45 | High-REE dol carb | -3.0 | 9.0 |
| CDD2-26 | CDD2 | 225.2 | High-REE dol carb | -3.3 | 20.8 |
| CDD1-31 | CDD1 | 269.5 | High-REE ap-mz rock | -3.1 | 15.5 |
| CDD1-37A | CDD1 | 270.3 | High-REE ap-mz rock | -3.5 | 10.5 |
| CDD1-37B | CDD1 | 270.3 | Dol carb | -2.9 | 9.1 |
| CDD2-5 | CDD2 | 92.9–93 | Ap-phl phoscorite | -3.9 | 10.1 |
| CDD2-11 | CDD2 | 220.6–220.7 | Clinopyroxenite | -5.4 | 11.3 |
| CDD2-14 | CDD2 | 250.85–251 | Clinopyroxenite | -5.6 | 11.1 |
| CDD2-17A | CDD2 | 293.6–293.79 | Clinopyroxenite | -4.4 | 11.2 |
| CDD2-23 | CDD2 | 231.12–231.44 | Clinopyroxenite | -4.2 | 9.7 |
| CDD2-24 | CDD2 | 309.85–310.06 | Clinopyroxenite | -3.8 | 21.4 |
| Mt Weld-88A | | | Mt Weld carbonatite | -4.2 | 12.9 |
| Mt Weld-88B | | | Mt Weld carbonatite | -4.2 | 12.9 |
| Mt Weld-1 | | | Mt Weld carbonatite | -5.6 | 8.9 |
| Mt Weld-2 | | | Mt Weld carbonatite | -5.4 | 7.2 |
| Mt Weld-87A | | | Mt Weld carbonatite | -5.6 | 6.3 |
| Mt Weld-87B | | | Mt Weld carbonatite | -5.5 | 6.6 |

**Table 6** $H_2O$-contents ("$H_2O$", in ppm) and stable hydrogen isotope compositions of fluid inclusion-hosted $H_2O$ (in ‰ relative to V-SMOW), as well as bulk carbonate C and O isotope compositions (in ‰ relative to V-PDB and V-SMOW, respectively) for ten carbonate samples from the Cummins Range carbonatites.

| Sample No. | Hole No. | Depth (m) | Rock type | $H_2O$ | δD | $\delta^{13}C$ | $\delta^{18}O$ |
|---|---|---|---|---|---|---|---|
| CDD2-1 | CDD2 | 69.5–69.65 | Low-Sr dol carb | 2466 | -38 | -4.1 | 20.9 |
| CDD2-3 | CDD2 | 82.25–82.4 | High-Sr cc carb | 737 | -41 | -4.1 | 8.3 |
| CDD2-6 | CDD2 | 113.9–114 | High-Sr dol carb | 932 | -35 | -3.0 | 8.7 |
| CDD2-7 | CDD2 | 128.15–128.3 | High-Sr cc carb | 1749 | -34 | -4.1 | 8.8 |
| CDD2-9 | CDD2 | 178.05–178.15 | High-Sr cc carb | 1431 | -40 | -4.0 | 8.5 |
| CDD2-10 | CDD2 | 199–199.15 | Low-Sr dol carb | 1909 | -54 | -4.2 | 21.7 |
| CDD2-12 | CDD2 | 225.65–225.8 | Low-Sr dol carb | 2110 | -49 | -3.6 | 21.0 |
| CDD2-18 | CDD2 | 328.78–328.94 | Low-Sr dol carb | 1119 | -47 | -4.2 | 21.9 |
| CDD2-19 | CDD2 | 370–370.15 | Low-Sr dol carb | 907 | -43 | -4.3 | 20.8 |
| CDD2-22 | CDD2 | 401.9–402 | High-Sr cc carb | 489 | -51 | -4.2 | 7.5 |

Supplementary Material

Click here to download Supplementary Material: Supplementary data Appendix 1.xlsx